Materials Today Physics 17 (2021) 100343

Contents lists available at ScienceDirect

Materials Today Physics

journal homepage: https://www.journals.elsevier.com/materials-today-physics

Plasmonic hybrids of two-dimensional transition metal dichalcogenides and nanoscale metals: Architectures, enhanced optical properties and devices

Y. Yang [a, *], W.G. liu [a], Z.T. Lin [a], R.H. Pan [a], C.Z. Gu [a, b], J.J. Li [a, b, c, **]

[a] Beijing National Laboratory for Condensed Matter Physics, Institute of Physics, Chinese Academy of Sciences, Beijing, 100190, PR China
[b] School of Physical Sciences, University of Chinese Academy of Sciences, Beijing, 100049, PR China
[c] Songshan Lake Materials Laboratory, Dongguan, Guangdong, 523808, China

ARTICLE INFO

Article history:
Received 11 November 2020
Received in revised form
23 December 2020
Accepted 4 January 2021
Available online 8 January 2021

Keywords:
Transition metal dichalcogenides
Nanoscale metals
Plasmonic hybrids
Architectures
Enhanced optical properties
Device applications

ABSTRACT

Hybridized with plasmonic nanoscale metals, including metallic nanoparticles and nanostructures, two-dimensional transition metal dichalcogenides (TMDs) exhibit unique enhanced optical properties, promising widespread applications in optoelectronic devices, such as photodetectors, photovoltaics and light-emitting devices. In this review, the recent developments of the plasmonic hybrids composed of TMDs and nanoscale metals are comprehensively described. First, the architectures of hybrid heterostructures are classified according to the stack site of TMDs, as well as the morphology of nanoscale metals. Then, the mechanisms behind the enhanced optical properties of plasmonic hybrids are briefly introduced. Furthermore, we elaborate the unique enhanced or tailored optical properties and the enabled applications of the hybrids of TMDs and nanoscale metals based on their architectures. Lastly, the prospect for the future fabrication trend and practical applications of the plasmonic hybrids are presented.

© 2021 Elsevier Ltd. All rights reserved.

1. Introduction

In recent years, two dimensional (2D) transition metal dichalcogenides (TMDs) have received plenty research interests, due to their novel optoelectronic properties and applications in light emitting, photodetection and sensor devices [1,2]. TMDs have a general chemical formula of MX_2, where M is a transition metal atom from groups IV, V, and VI, and X is a chalcogen atom [3,4]. In particular, molybdenum- and tungsten-based TMDs are semiconductors, having indirect band gaps ranging from the visible to the near-infrared (NIR) in bulk forms. Remarkably, TMDs exhibit larger direct band gap (1.7–2.2 eV) when they are thinned down to monolayers [5]. Compared with graphene that has a gapless band structure and hence has limitations in the applications of electric transistors and photodetectors, the bandgap of TMDs is in the NIR-to-visible range, shows superiority in the integration into optoelectronics devices, such as light-emitters, photodetectors and modulators [6–9]. The semiconducting characteristics of TMDs results in a well-defined boundary between their on and off states which is very useful in a device operation. In addition, their atomically thin feature enables high transparency, mechanical flexibility, easy fabrication and integration, and robustness, offering the opportunity for bendable, flexible, and conformal devices, and new optoelectronics emerging wearable and portable optoelectronics [7,10].

However, the thickness of 2D TMDs is too thin to absorb sufficient light, which inevitably restricts their efficient applications in optoelectronics. For example, the light absorption of monolayer MoS_2 is less than <10% [11,12], although its already much higher than that of graphene (2.3%) [13]. Due to the limited light-harvest ability and manipulating possibility, efficient utilizations of TMDs are far from practical applications. Thus, efficiently enhancing the light absorption of TMDs materials to satisfy the requirements of practical applications has become an important issue.

To solve this problem, integrating TMDs with plasmonic nanoscale metals, including metallic nanoparticles and nanostructures, has been demonstrated to be a novel strategy to broaden the application of TMDs. Plasmonic nanoscale metals enable light

* Corresponding author.
** Corresponding author. Beijing National Laboratory for Condensed Matter Physics, Institute of Physics, Chinese Academy of Sciences, Beijing, 100190, PR China.
E-mail addresses: yang.yang@iphy.ac.cn (Y. Yang), jjli@iphy.ac.cn (J.J. Li).

https://doi.org/10.1016/j.mtphys.2021.100343
2542-5293/© 2021 Elsevier Ltd. All rights reserved.

manipulation beyond the diffraction limit of light by the excitation of surface plasmons, which confines the electromagnetic field at the interface between semiconductors and metal, have been demonstrated to improve the performance of semiconductor optoelectronic devices [14–16]. Due to the plasmonic light-mater interaction, the light-harvesting efficiency and optical responds of TMDs are significantly enhanced, so the plasmonic TMDs hybrids show exceptional potential applications in optoelectronics as a result. With the advance of nanomaterial synthesis and the progress of nanofabrication techniques, researchers have achieved substantial progress toward such a goal in the past years.

In recent years, several articles have reviewed the progress in the research on the hybrids of 2D materials and metallic nanomaterials [17–21], however, which normally emphasized on a certain topic, and a more comprehensive and in-depth review is needed. As we know, the optical properties and device application of the plasmonic hybrid nanosystems closely depend on their architecture structures, and hence around the different architecture structures of the TMDs-nanoscale metals hybrids, their related enhanced optical properties and device applications should be symmetrically discussed.

In this review, we provide an overview of the recent research on the TMDs-nanoscale metals hybrids, based on their various architectures, the plasmon enhanced optical properties and the applications in optoelectronic devices, as summarized in the Fig. 1. Particularly, the architectures of the plasmonic hybrid heterostructures is firstly classified, and the mechanisms behind the enhanced optical properties of the plasmonic hybrid heterostructures is briefly discussed in Section 2. Further, the enhanced optical properties of TMDs, including photoluminescence (PL) emission, reflectance, absorbance, Raman spectra and nonlinearly optical property are presented and discussed based on the architecture of the plasmonic hybrids in Section 3. The device applications of the plamonic hybrid nanosystems are reviewed in Section 4. Finally, the conclusion and outlook for future development and potential applications of hybrids of TMDs-nanoscale metals are discussed in Section 5.

2. Architectures of plasmonic hybrids of TMDs and nanoscale metals

2.1. Architectures of plasmonic hybrids

Before discussing the architectures of the hybrids of TMDs and nanoscale metals, the following points should be addressed in advance. (1) Although there are many methods for preparing

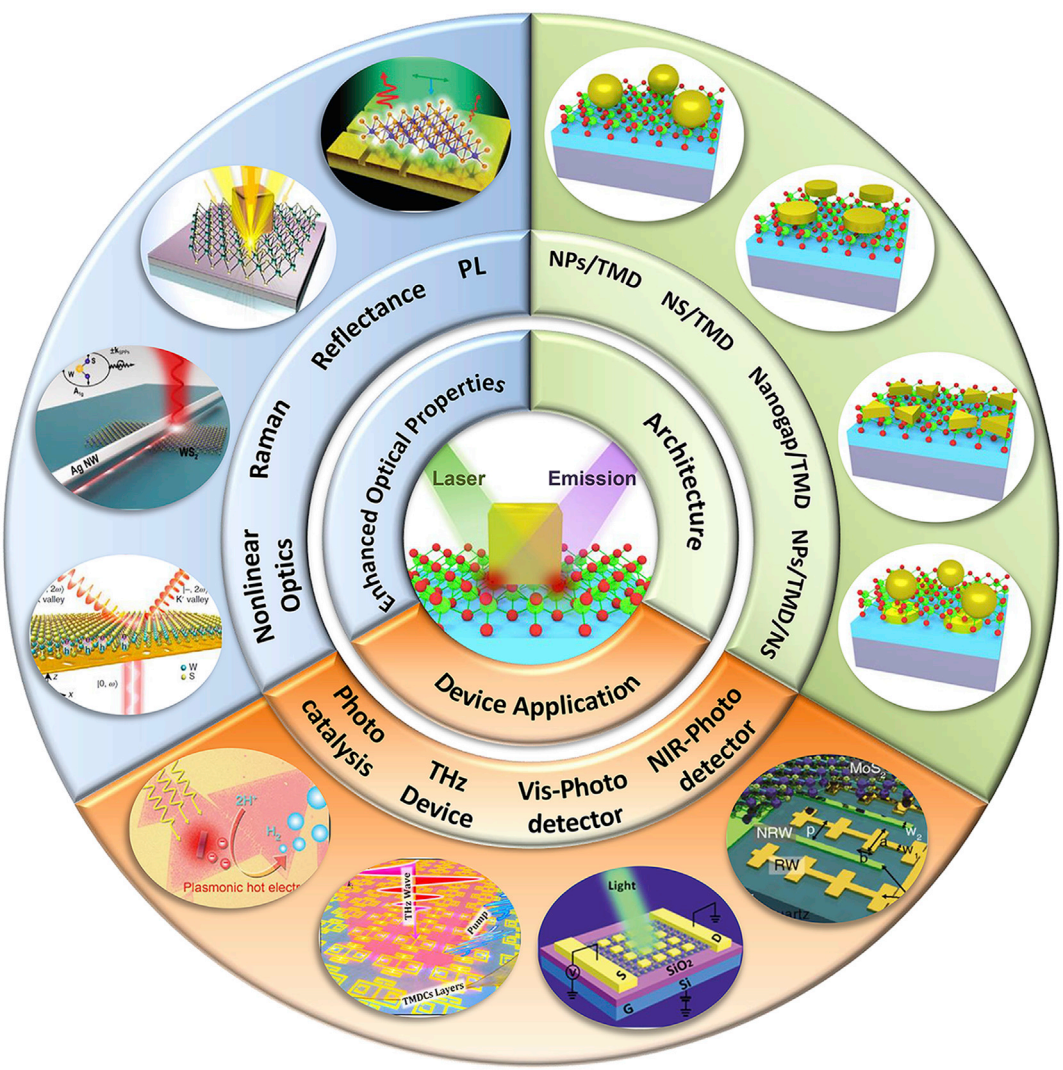

Fig. 1. Summary of the architectures, enhanced optical properties and devices applications for the plasmonic hybrids of TMDs and nanoscale metals.

monolayer and few-layer TMDs, the mechanically exfoliated (ME) and chemical vapor deposition (CVD) grown TMDs are the mostly employed for constructing plasmonic hybrids, because a flat 2D TMDs flake is essential for forming a photoelectric device, especially to integrate with silicon technologies [22–24]. In addition, the intrinsic physical properties of ME TMDs or CVD TMDs can be best reserved than the TMDs prepared by other methods, guaranteeing their applications in high performance photoelectric devices [25–27]. (2) Two types of nanoscale metals including metal nanoparticles (NPs) and metal nanostructures (NSs) are discussed in this review. In this review, NPs are random and prepared using chemical synthesis and physical deposition methods, whereas the NSs are periodic and fabricated using planar micro/nanofabrication techniques.

Plasmonic NPs include usually different morphologies, such as not only irregular-shaped nanoparticles, but also nanocubes, nanospheres, nanotriangles, etc [28–30]. For the sake of discussion, some randomly distributed nanomaterials with large aspect ratio [31–33], such as nanorods, nanowires, are classified as NPs, which are also used to compose hybrid heterostructures with TMDs as well. On the other hand, most plasmonic NSs are the regular periodic nanostructures, such as nanodisks, nanopillars and nanopores, etc [34–37]. Except from the above, nanogap is considered as a special type of NSs to be combined with TMDs, which can greatly boost local electromagnetic (EM) field for enhanced optical properties of the hybrids [38,39]. Particularly, in order to promote the application of TMDs in THz devices or nonlinearly optical devices, the metasurfaces with specific patterns based on NSs are designed to couple with TMDs.

Most NPs are prepared using the so-called seed-mediated method, has become the most popular approach to synthesize NPs with different morphologies [40]. To constitute hybrids with TMDs, NPs are randomly dispersed on the substrate or on the surface of TMDs. In addition to the randomly dispersed NPs, periodic organized NPs arrays can be fabricated using template methods, such as anodic aluminum oxide (AAO) template and sphere lithography [41,42]. Except from chemical methods, physical methods, including sputter deposition, thermal evaporation, and electron-beam evaporation with the aid of the annealing process, also are used to fabricate NPs over large area. By controlling the deposition rate and time, the size and density of NPs can be modulated. The periodic NSs are fabricated using nanofabrication techniques that are widely employed in fabricating plasmonic nanostructures, such as optical lithography, E-beam lithography (EBL), focused ion beam (FIB) etching, reaction ion etching (RIE), etc.

In contrast to the freestanding NSs that pursue the highest plasmonic enhancement and need special fabrication procedure, the NSs utilized in this hybridization are relatively simple and mostly focused on how to better integrate with TMDs.

2D TMDs and nanoscale metals can constitute various hybrid heterostructures, as summarized and classified in the Fig. 2. Generally speaking, there are two types of hybrid architectures, (1) double-layer architecture composed of one layer of nanoscale metals and a TMDs flake, (2) three-layer sandwich-like hybrid nanostructure composed of nanoscale metals, TMDs, and a mirror metal layer (or NSs), in which the TMDs layer is inserted in the middle. As presented in Fig. 2(a), NPs can be deposited on or underneath the TMDs layers, for the double-layer TMDs-NPs hybrids. Similarly, in the double-layer TMDs-NSs hybrids, NSs can be fabricated after or before transferring TMDs, as presented in Fig. 2(b). In addition to the regular periodic NSs, NSs with special structure designs are proposed, and the selected schematics of three typical hybrids are exhibited in Fig. 2(c), such as nanopillars, nanopore, nanogap. Nanopillars as a high aspect ratio NS are employed to support TMDs, and nanopore arrays are also often fabricated as sunken NS under TMDs. Among various NSs, nanogaps array is special nanostructure due to its strong local EM field, which are fabricated to hybridize with TMDs for outstanding enhanced optical properties. For three-layer sandwich-liked hybrids, a metal film is mostly deposited as a mirror layer before transferring TMDs, and NPs or NSs are then deposited on top of TMDs, as illustrated in Fig. 2(d). Of course, the mirror layer can be replaced by NSs in some specified applications.

From the view-point of the feasibility, double-layer architectures are mostly employed in the fabrication of plasmonic hybrid frameworks, but the sandwich-liked architectures pave an additional route for plasmonic enhancement in the hybrids though complicated in fabrication process [43,44]. Moreover, the mechanisms under the plasmonic enhancement of TMDs-nanoscale metals hybrids depend on the architecture structures, and the optical properties of TMDs can be enhanced and modulated as a result. Additional plasmonic enhancement can be introduced into the sandwich-liked hybrid frameworks by placing the mirror layer underneath TMDs. In the following section, the mechanisms under the enhanced optical properties of the plamonic hybrids will be discussed.

2.2. Mechanisms under the enhanced optical properties of the hybrids of TMDs and nanoscale metals

The optical responses of the TMDs layers can be dramatically modulated by the hybrids of plasmonic nanoscale metals and TMDs. The plasmonic structures improve optical absorption in the TMDs layer through three path [45] (i) scattering the incident ray of light, which increases the interaction length; (ii) trapping light by excitation of localized surface plasmon resonances (LSPRs), which enhances the absorption cross section. or (iii) trapping and guiding light via surface plasmon polaritons (SPPs) at the metal semiconductor interface, which increases the interaction length and cross section. Among above TMDs-nanoscale metals interaction mechanisms in hybrids, LSPRs play the dominant role in the modulated optical properties of TMDs in both double-layer and three layer architectures [17–21]. On the other hand, the SPPs normally take place in a continuous metal layer, consequently influencing the enhanced optical properties, especially in the sandwich-liked hybrids.

LSPRs, induced by the collective oscillation of electrons in the metal surface, can be excited by far-field incident light, whose energy can be consequentially concentrated at the surface of NPs and NSs [46–48]. While the frequency of the incident light wave is in resonance with the characteristic frequency of LSPRs, the local EM field is prominently enhanced as a result. The intensity of the excited light, which is proportional to the square of the amplitude of EM field ($\boldsymbol{E}$), can be enhanced by 2-5 orders of magnitude. The low absorption efficiency of TMDs can be increased, and thus the photoelectronic covert yield of the TMDs can be significantly boosted as a result, as the schematic drawing exhibited in Fig. 3(a). In addition to the high enhancement factor, one advance of LSPRs over SPPs is less dissipation since the induced EM wave is locally confined and cannot propagate along the metal surface [15]. In the strong coupling process of TMDs' excitons and surface plasmon, the spontaneous emission rate for the 2D TMDs layer is also enhanced as a result of the increased internal quantum efficiencies and promoted radiative decay, which is known as the Purcell effect [49–52]. When the resonant frequency of the LSPRs overlaps the emission frequency of the TMDs, the PL energy coupled to the LSPRs mode is prominently increased [31]. The effective enhancement of the plasmonic nanostructures on the PL emission of TMDs should be a product of the enhancement of excitation and emission. Designing and fabricating proper nanostructures with high EM

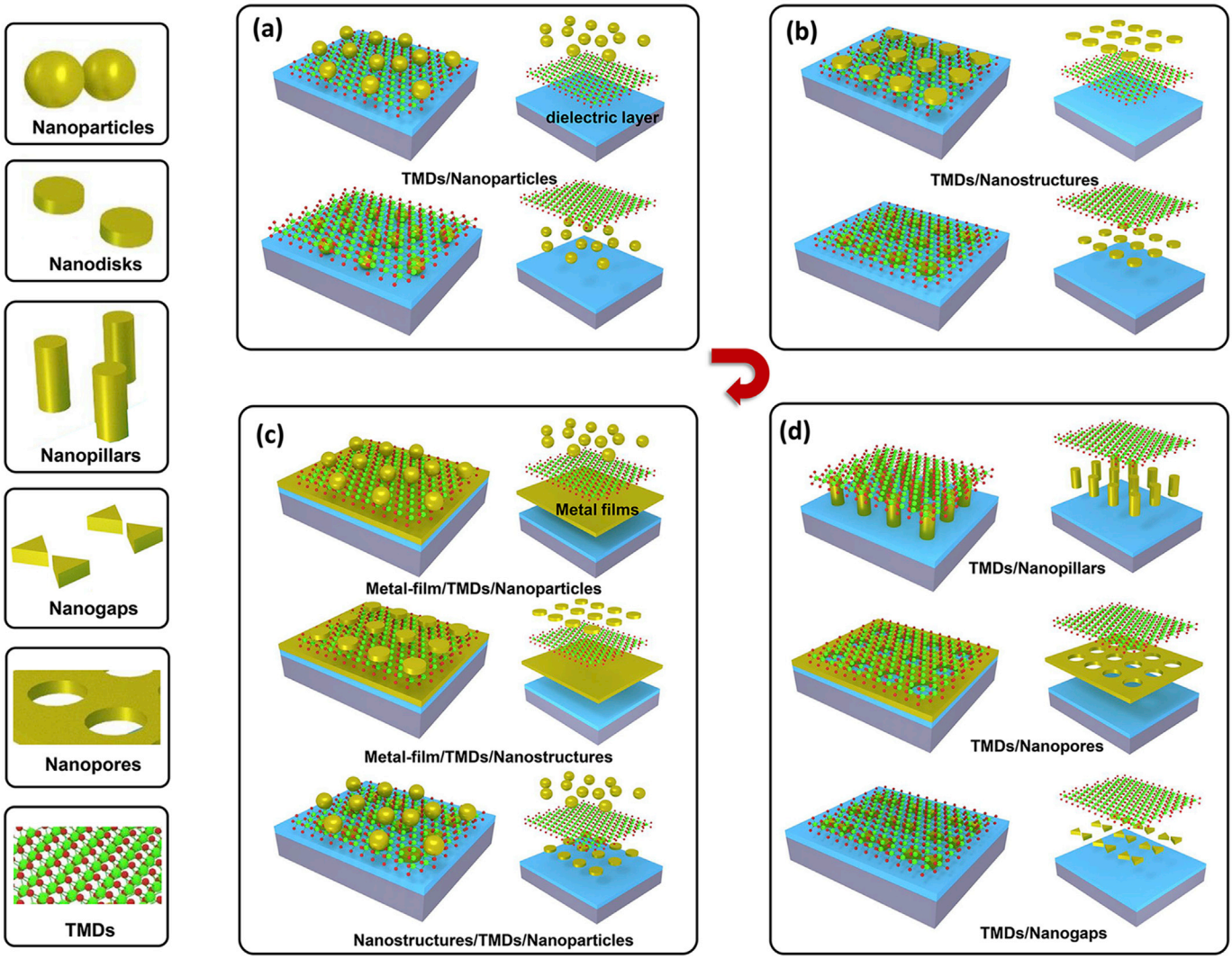

Fig. 2. Schematic drawings of different architecture types of plasmonic hybrids of TMDs and nanoscale metals, and some typical structural units are shown on the left, including nanoparticles and nanostructures with nanodisks, nanopillars, nanogaps and nanopores. (a) double-layer architecture composed of random NPs and TMDs, (b) double-layer architecture composed of periodically arrayed NSs (nanodisks as an example) and TMDs, (c) double layer architecture composed of NSs with special geometries and TMDs, which are nanopillars, nanopores and nanogaps from top to bottom, (d) three-layer architecture with sandwich-like plasmonic hybrid composed of nanoscale metals, TMDs, and a mirror metal layer (or periodic NSs).

enhancement in both excitation and emission wavelength range is the key to achieve the best performance for plasmonic TMDs hybrids.

Another important property of plasmonic nanoscale metals is their ability to generate energetic or “hot” carriers under an excitation light, which can enable photocurrent generation from photons with energy below the bandgap of the 2D semiconducting channel [53–59]. For the PL emission process of the semiconducting TMDs, PL light is emitted during the recombination of excitons. The excitons are formed by the electrons those relax from the conduction band into the excitonic level, which are excited by the laser with a proper wavelength. In the TMDs/nanoscale metals, the surface plasmon excited "hot electrons" inject into the conduction band of the semiconducting TMDs, resulting to significantly increased density of excitons, and enhance the PL emission of TMDs consequently, as illustrated in Fig. 3(b).

As known, the free electrons oscillate collectively at the metal surface to form LSPRs. Due to Landau damping, the in-phase oscillation gradually becomes diphase, and non-equilibrium electron distribution is formed consequently. The energy between high-energy electrons and those with low energy exchanges because of the electron-electron scattering, giving rise to a Fermi-Dirac-like electron distribution, so-called as hot electron distribution [17]. The incident light can couple with surface plasmons by nanoantennas, and the nonradiative decay of the plasmons results in hot electrons that can transfer across the Schottky barrier at the metal–semiconductor interface and be detected as a photocurrent [53,54]. The generation of “hot electrons” in plasmonic TMDs-nanoscale metals hybrids play a significant role in enhancing the performance of photoelectric and photocatalysis devices [55–58].

For three-layer sandwich-like hybrids, the coupling effect between the LSPR and SPPs will play an important role in the mechanisms under the enhanced optical properties of TMDs [60–62]. When an ultra-thin nanogap is constructed by inserting a layer of TMDs between NPs (or NSs) and a metal layer, a so-called nanocavity is produced as well. The coupling between the LSPR on NPs (or NSs) and the SPPs of metal layer can significantly enhance the EM field in the gap region, as illustrated in Fig. 3(c). The PL emission of TMDs can be significantly enhanced due to the exciton-coupled SPPs that propagate from the metal film [43,44].

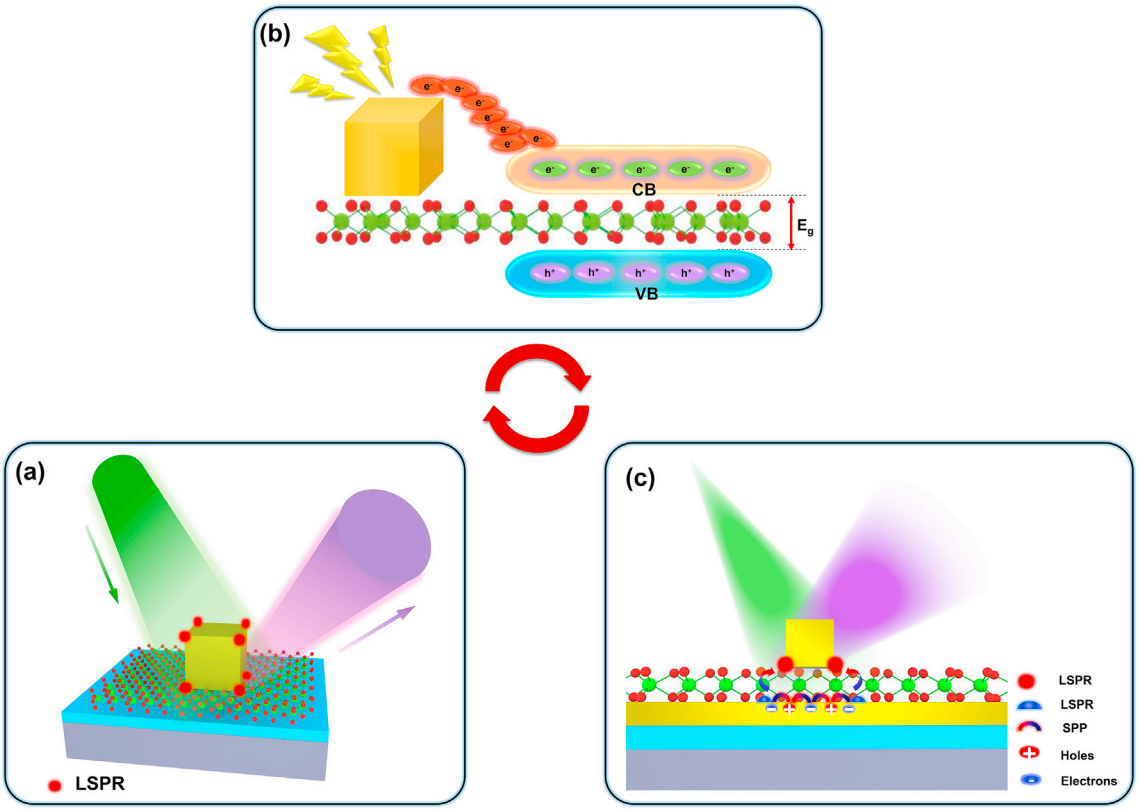

Fig. 3. Schematic illustration of three typical mechanisms under the enhanced optical properties of the hybrids. (a) LSPR coupling with PL emission, (b) hot-carrier effect and (c) the coupling effect between LSPR and SPPs in the plasmonic hybrid of nanoscale metals and TMDs.

The SPPs of the nanocavity can be tuned by controlling the thickness of nanogap and the size of NPs, which allows to successively adjust the SPPs to accurately match the exciton energy of TMDs [63].

In addition to the prominent field enhancement characteristic, periodic plasmonic NSs show unique resonance coupling efficiency with high quality factor, which makes them a suitable candidate to achieve coherent coupling between excitons and plasmons in the system of TMDs-NSs hybrids. Thanks to the development of nanofabrication techniques, metal NSs with controllable periods, size, and the shape have been successfully fabricated. In the strong coupling process of exciton and surface plasmon, splitting in the spectra, so-called Rabi splitting, can also be observed [64,65]. This is essential for fabricating an emitter with a high oscillator strength and a high exciton binding energy [64]. Strongest coupling between exciton and plasmon is achieved when LSPRs locate in the resonance with MoS_2 excitons and detuned lattice resonances [66,67].

The exciton-plasmon coupling in hybrid TMDs-nanoscale metals effectively modulates the optical properties of TMDs. Through coupling between excitons, LSPRs of the nanostructures, emission quantum efficiency of TMDs significantly improved, novel 2D plasmonic polaritonic devices can be realized.

3. Enhanced optical properties of plasmonic hybrids

The optical properties, such as PL emission, reflectance, absorbance and Raman scattering of TMDs can be significantly improved after hybridized with nanoscale metals. In the following section, the enhanced optical properties of plamonic hybrid of TMDs-nanoscale metals will be discussed based on their architecture configurations.

3.1. Enhanced photoluminescence (PL) of different hybrid frameworks

The most widely studied optical property of TMDs is the PL emission, therefore diverse nanoscale metals have been employed to hybridize with TMDs in order to enhance their PL emission. In this section, the enhanced PL property of TMDs-nanoscale metals hybrid nanosystems will be discussed based on five types of architectures, including four types of double-layer architecture, such as NPs on or under TMDs (NPs/TMDs and TMDs/NPs), NSs on or under TMDs (NSs/TMDs and TMDs/NSs), and the three-layer sandwich-like architecture.

3.1.1. Decorating nanoparticles on TMDs (NPs/TMDs)

Firstly, the plasmonic hybrid frameworks composed by randomly dispersing NPs on the surface of TMDs (NPs/TMDs) are introduced in Fig. 4. NPs are the most frequently used to generate LSPRs due to their advances in various morphology, rapid synthesis, high-throughput and low cost, and undoubtedly employed to form plasmonic hybrids with TMDs [28,29,32]. In 2016, Cao et al. systematically studied the influences of the morphology of nanoparticles on the PL emission of MoS_2 [30]. A library of Ag nanoparticles, including shape-controlled cubes (Ag NC), octahedra (Ag OCT), and spherical particles (Ag SP) of various sizes were employed to tailor the light-mater interaction. The optical images of single Ag NC and Ag OCT covered MoS_2 are shown as an example in Fig. 4(a)-i. The PL maps in Fig. 4(a)-ii clearly exhibited that the PL intensity Ag NC and OCT are significant different from each other. The PL for Ag NC/MoS_2 was enhanced by ~2 times, whereas the PL for Ag OCT/MoS_2 was weakened to 50%, as shown in Fig. 4(a)-iii and 4(a)-iv. The quenching of PL for Ag OCT/MoS_2 can be attributed to

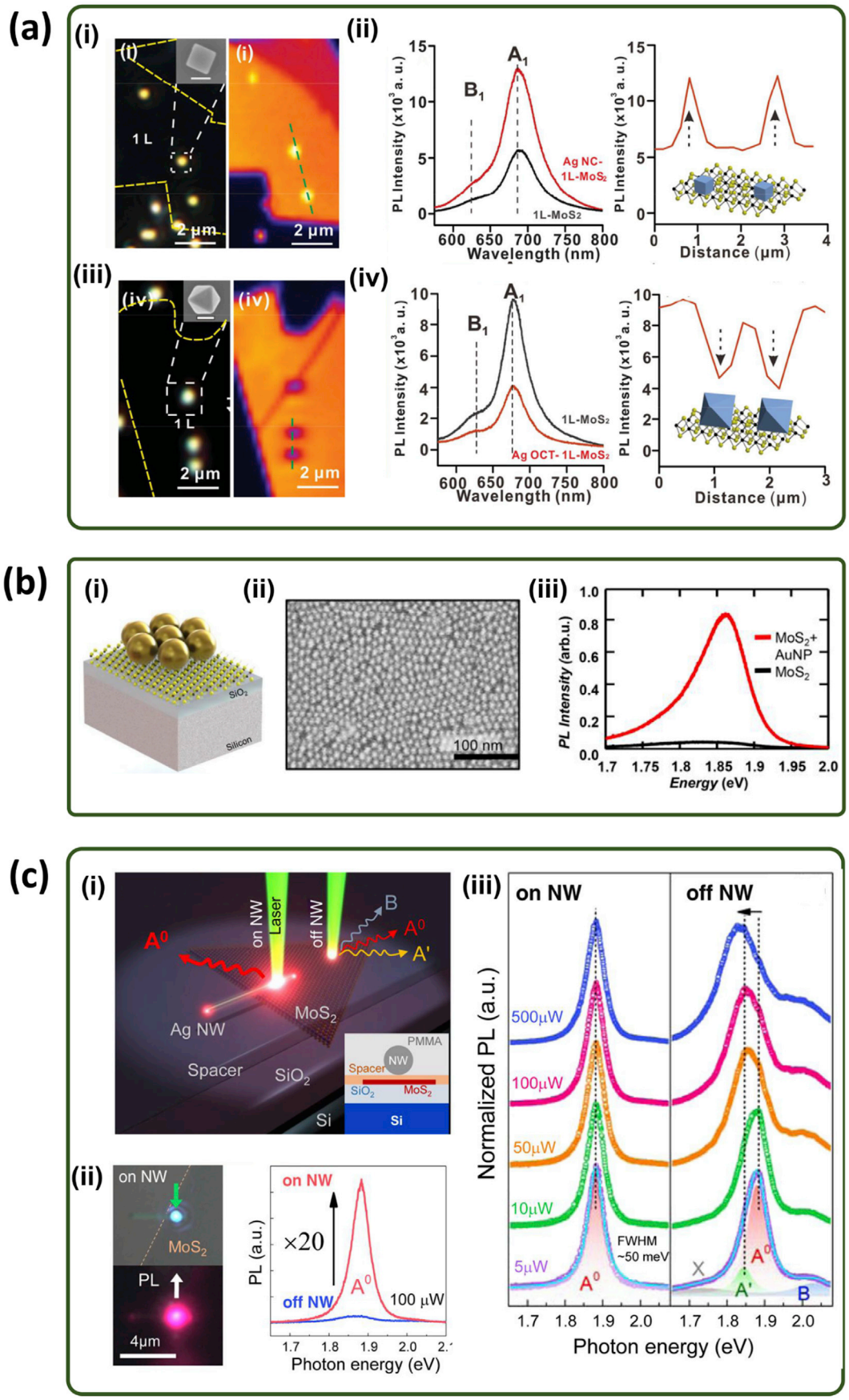
(a)
(i)
(ii)
(iii)
(iv)
1 L
2 μm
A1
B1
Ag NC-1L-MoS2
1L-MoS2
Ag OCT-1L-MoS2
PL Intensity (x10³ a. u.)
Wavelength (nm)
Distance (μm)
(b)
(i)
(ii)
(iii)
SiO2
Silicon
100 nm
MoS2+AuNP
MoS2
PL Intensity (arb.u.)
Energy (eV)
(c)
(i)
on NW
off NW
Laser
A0
B
A'
Ag NW
MoS2
Spacer
SiO2
Si
PMMA
NW
(ii)
on NW
MoS2
PL
4μm
×20
off NW
100 μW
PL (a.u.)
Photon energy (eV)
(iii)
on NW
off NW
Normalized PL (a.u.)
500μW
100μW
50μW
10μW
5μW
FWHM ~50 meV
X
A'
B
Photon energy (eV)

the reduced quantum yield (0.2-fold) and collection efficiency (0.26%) due to the poor directionality of high order plasmon modes.

Except dispersed nanoparticles, close-packed nanoparticles were also used in the preparation of hybrid structure. Diefenbach et al. proposed a hybrid structure in which monolayer Au-NPs were decorated on the surface of monolayer MoS_2, as illustrated in Fig. 4(b)-i [33]. The close-packed Au-NPs arrays were formed by fast evaporation of the Au-NP solvent that was dropped on a convex air-water interface and subsequent convective flow (see Fig. 4(b)-ii), then transferred to the Au-NP arrays on top of monolayer MoS_2 via microcontact printing with a PDMS stamp. As presented in Fig. 4(b)-iii, the PL intensity of MoS_2 was significantly enhanced by a factor of up to 20 after decorated with Au-NPs.

Besides 0 D nanoparticles, 1D metallic nanorods and nanowires (NW) were also selected to enhance the PL of TMDs [31,32,68]. Lee et al. proposed a method of selectively amplifying the primary exciton (A_0) among the exciton complexes in monolayer MoS_2 via cyclic reexcitation of cavity-free exciton-coupled plasmon propagation [69]. As exhibited in Fig. 4(c)-i, the plasmonic hybrid framework was implemented by partially overlapping a Ag nanowire on a MoS_2 monolayer separated by a thin SiO_2 spacer. The PL image in Fig. 4(c)-ii exhibits a strong red emission at the laser input position (LIP) indicated by a green arrow and a weak but still prominent emission at the NW-end position, implying that MoS_2 excitons were coupled to SPPs and propagated along the NW. Notably, the A_0 was dramatically enhanced compared with that for off NW, with an enhancement factor of ~20 (right panel in Fig. 4(c)-ii). Fig. 4(c)-iii shows the normalized PL spectra that were deconvoluted using a Lorentzian function. For on NW, only the A-peak was observed, and full width at half maximum of ~50 meV remained unchanged and independent of excitation power (P_{ex}). In contrast, for off NW, as P_{ex} increased, the A-peak center position redshifted considerably because the A_0 dominates the A peak, and the intensities of A_0 and B increase.

Although diverse NPs have been synthesized by the chemical method, physical method is another route to prepare NPs, which have also been employed to enhance the PL emission of TMDs [70–73]. By employing a focused micro-power laser beam, silver NPs can be rapidly (in seconds) anchored onto the irradiated area of MoS_2 flakes, forming 0D/2D AgNPs@MoS_2 heterostructures [71].

3.1.2. Transferring TMDs on nanoparticles (TMDs/NPs)

Besides directly dispersing NPs on TMDs, transferring TMDs on the substrate with previously decorated NPs (TMDs/NPs) has also been demonstrated to be a feasible strategy to fabricate plasmonic hybrid nanosystems [74,75]. As illustrated in Fig. 5(a)-i, a hybrid framework with the PL enhancement of 200 times was built by transferring CVD-grown MoS_2 on Au NPs arrays [53]. As shown in Fig. 5(a)-ii, the Au NPs with a diameter of 10 nm self-assembled into a uniform sub-monolayer, with a density of 240 NPs μm^{-2}. The density of Au NPs can be increased by the PMMA-assisted wet-transferring technique. As exhibited in Fig. 5(a)-iii, the PL intensity enhancement did not monotonically depend upon the density of Au NPs. Using Ag NWs network as plasmonic hybrid composite, the PL of MoS_2 can be enhanced by 560 times [76]. Cai et al. demonstrated the coupling of single localized defects in monolayer WSe_2 self-aligned to the surface plasmon mode of a silver NW, in which an average coupling efficiency with a lower bound of 26% ± 11% was achieved [77].

Chemical synthetic methods are efficient in high-throughput fabrication of plasmonic dimers [78], but suffer from poor control over the assembly patterns due to aggregation of the colloidal particles. In order to overcome this disadvantage of colloidal particles, Hao and co-workers fabricated a hybrid heterostructure by transferring MoS_2 on patterned plasmonic dimers those were obtained by utilizing porous AAO templates during angle-resolved shadow deposition (see Fig. 5(b)-i) [79]. As the high resolution SEM displayed in Fig. 5(b)-ii, the plasmonic dimers are with uniform size, well-defined orientation and sub-10 nm gaps. The PL intensity from MoS_2-dimers hybrid is enhanced by up to a factor of ~160 by resonant excitation of the dimer modes, as shown in Fig. 5(b)-iii. The PL exhibited strong dependence on the polarization of incidence laser due to the strongly confined EM fields in the vicinity of the dimer gaps.

In addition to linear polarized light, valley-dependent circular polarized light (chiral light) can be modulated using a hybrid plasmonic nanosystem. In 2019, Ding et al. proposed a type of hybrid plasmonic structure to tune the valley polarized PL in monolayer WS_2 [80]. Fig. 5(c)-i shows the scheme of the monolayer WS_2 transferred onto the top of the plamonic crystals (PCs). The PCs were fabricated by depositing Ag film on the closely packed silica spheres with a diameter of ~425 nm (±5%), which were then coated with a thin SiO_2 layer for protection. Fig. 5(c)-ii exhibits the SEM image of the WS_2/PC hybrid, but it was difficult to identify the presence of WS_2 due to its ultrathin thickness. The PL helicity in WS_2/PC hybrid was sensitive to the excitation angle of the pump beam, as shown in Fig. 5(c)-iii. This is contrast to that of the PL helicity of bare WS_2, which showed no change to excitation angles.

NPs prepared using physical methods have also been in TMDs/NPs hybrid frameworks. A creation of strain induced single photon sources using a WSe_2 monolayer on silver islands was reported [81]. Quantum emitters were formed by hybridizing with Ag nanoparticles on rough Ag films, in which emission was highly linearly polarized, stable in linewidth, and decay times down to 100 ps were observed.

3.1.3. Integrating nanostructures on TMDs (NSs/TMDs)

Thirdly, utilizing advanced nanofabrication techniques, periodic NSs have been feasibly fabricated on top of TMDs (NSs/TMDs) [34,66,67,82]. The representative plasmonic hybrid nanosystems constructed by fabricating NSs on TMDs is discussed in Fig. 6. Li et al. proposed a hybrid structure in which periodic Ag nanoantenna arrays were fabricated on MoS_2 surface, as presented in Fig. 6(a)-i [35]. As shown in Fig. 6(a)-ii, the in-plane size of nanoantenna was ~40 × 80 nm, and its height was measured at ~ 35 nm by using AFM scanning. As displayed in Fig. 6(a)-iii, the PL enhancement of the hybrid showed obvious polarization angle dependence in addition to the intensity enhancement. The maximum enhancement was approaching 10 times when the incident polarization was of $\theta = 0°$.

It is well known that the resonance center of the plasmonic nanoarrays can be tuned by adjusting the size, shape, and period of the nanopatterns. Butun et al. fabricated nanodisc arrays on large area CVD deposited monolayer MoS_2, and modulated plasmonic resonance of the nanodisc arrays by the varying the diameter of the nanodiscs (see Fig. 6(b)-i) [83]. As presented in Fig. 6(b)-ii, PL for

Fig. 4. Enhanced PL of the hybrids composed by randomly dispersing NPs on the surface of TMDs (NPs/TMDs). (a) i: Dark-field optical microscope image ii: PL map image and iii: PL of exfoliated 1L-MoS_2 deposited with single Ag NC and Ag OCT. iv: A_1 band intensity profile across the NC and OCT particles. Reproduced with permission [30]. Copyright 2015, WILEY-VCH Verlag GmbH & Co. (b) i: Sketch of Au-NPs on top of a monolayer MoS_2. ii: SEM image of an Au-NP array on a SiO_2/Si substrate iii: PL spectra of a pristine MoS_2 and an Au-NP-decorated MoS_2. Reproduced with permission [33]. Copyright 2018, American Chemical Society. (c) i: Schematic of the experimental setup with a side view of the hybrid. ii: (Top) Optical micrograph showing the LIP. (Bottom) PL image showing the collection position of the PL signal at the same LIP. (Right) PL spectra for on NW and off NW. iii: Normalized PL signals as a function of P_{ex} for on NW and off NW. Reproduced with permission [69]. Copyright 2015, American Physical Society.

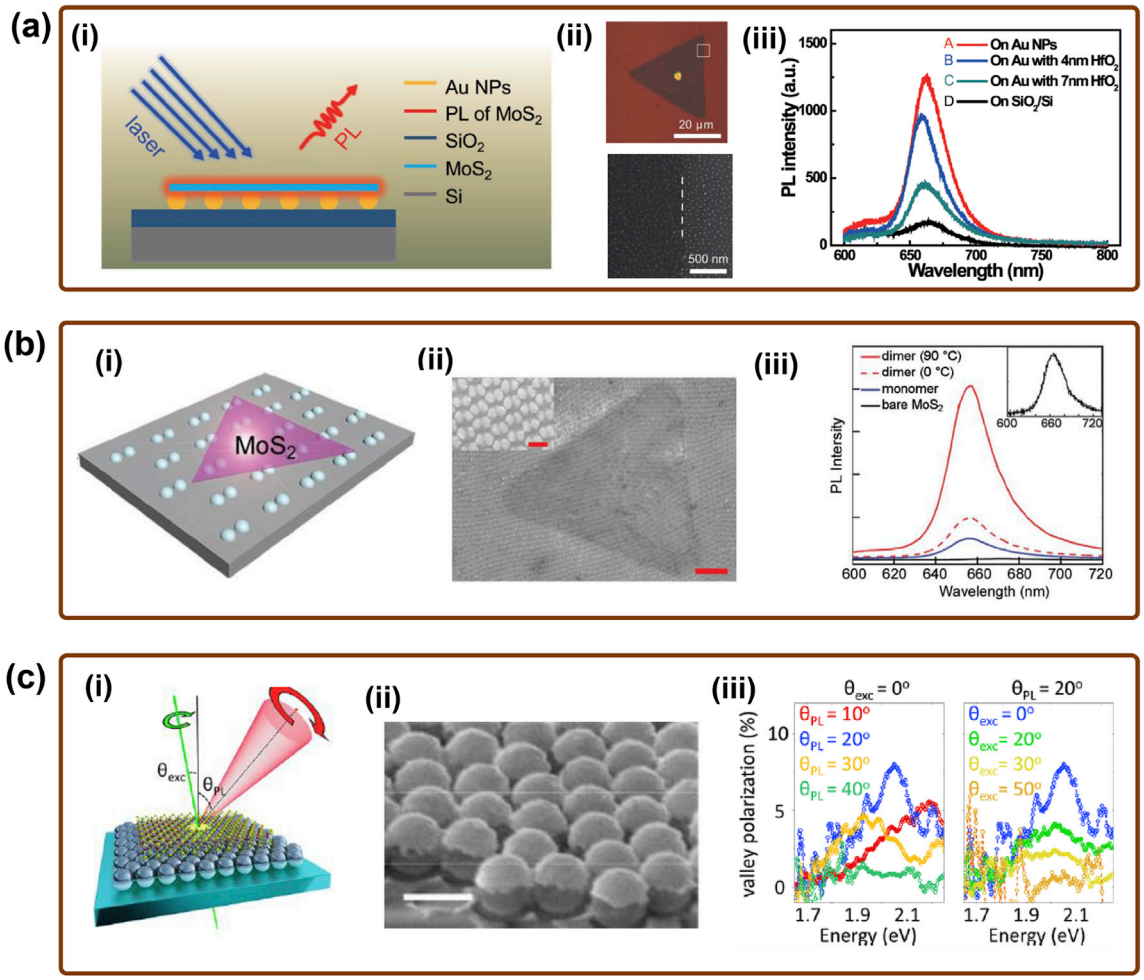

Fig. 5. Enhanced PL of plasmonic hybrids constituted by transferring TMDs on the substrate with previously deposited NPs (TMDs/NPs). (a) i: Schematic image of the sample structure showing the monolayer MoS_2 on the self-assembled Au NP array ii: Optical image of a monolayer MoS_2 on Au NPs. And SEM image of the area in the rectangular area marked in panel. iii: Typical PL spectra of MoS_2 on Au NPs with different densities. Reproduced with permission [53]. Copyright 2017, WILEY-VCH Verlag GmbH & Co. (b) i: Scheme of a monolayer MoS_2 transferred onto the dimer arrays. ii: SEM image of the fabricated nanodimer array with suspending monolayer MoS_2. The inset shows a high resolution SEM image of the plasmonic dimers with sub-10 nm gaps. iii: Typical PL spectra from bare MoS_2, the MoS_2/monomer, and MoS_2/dimers under polarized light parallel (90°) and perpendicular (180°) to the dimers axis. Reproduced with permission [79]. Copyright 2017, WILEY-VCH Verlag GmbH & Co. (c) i: Schematic of polarized PL experiment on the hybrid of WS_2/plasmonic crystal. ii: SEM image of a monolayer WS_2 on silica spheres coated with the Ag film. iii: Valley-polarized PL at different emission (θ_{PL}) and excitation angles (θ_{exc}). Reproduced with permission [80]. Copyright 2019, American Chemical Society.

the nanodisc-MoS_2 hybrids were always greater than pristine monolayers, of which the maximum intensity was achieved for diameter of 130 nm, about 12 times brighter. Fig. 6(b)-iii displays PL mapping under different excitation wavelength, clearly demonstrating that the resonance center varied while changing the diameter of nanodics.

It has been demonstrated that the dimer structure can significantly enhanced the LSPR compared with an isolated nanostructure, due to the extraordinary enhanced EM field in the nanogap [47,84,85]. So different dimer patterns have been fabricated and utilized to enhance the PL emission of TMDs [38,86]. As displayed in Fig. 6(c)-i and 6(c)-ii, 50 nm thick silver bowtie arrays with varying geometrical factors were patterned directly on the MoS_2 flakes via EBL [38]. As presented in Fig. 6(c)-iii, the PL intensity of bowtie-MoS_2 hybrid was enhanced by 40 times compared with bare MoS_2.

3.1.4. Covering TMDs on the nanostructures (TMDs/NSs)

Fourthly, different approaches have been developed to form plasmonic hybrid heterostructure by placing TMDs on the NSs previously fabricated (TMDs/NSs) in order to improve the PL emission enhancement [87–89]. Najmaei et al. have successfully fabricated a type of MoS_2-nanoantenna hybrid by transferring CVD-grown MoS_2 monolayer films on rectangular shaped nanoantenna arrays, as illustrated in Fig. 7(a)-i and (a)-ii [34]. Using a temperature calibration procedure based on photoluminescence spectral characteristics, the local temperature changes were able to be estimated. The plasmonically induced MoS_2 temperature increase is nearly four times larger than in the MoS_2 reference temperatures, as shown in Fig. 7(a)-iii.

The PL emission efficiency of TMDs can be raised by strain engineering, allowing their application in the quantum emitter, which can be employed as bright nonclassical light sources for applications in quantum communication and optical quantum computing. The giant PL enhancement in this kind of hybrid frameworks was attributed to the Purcell effect and increased light absorption. Metal nanopillars have been demonstrated to be a good candidate for composing quantum emitter by introducing strain in TMDs own to their high aspect ratio, in addition to their plasmonic enhancement [90]. Cai et al. proposed a platform for quantum emitter near the

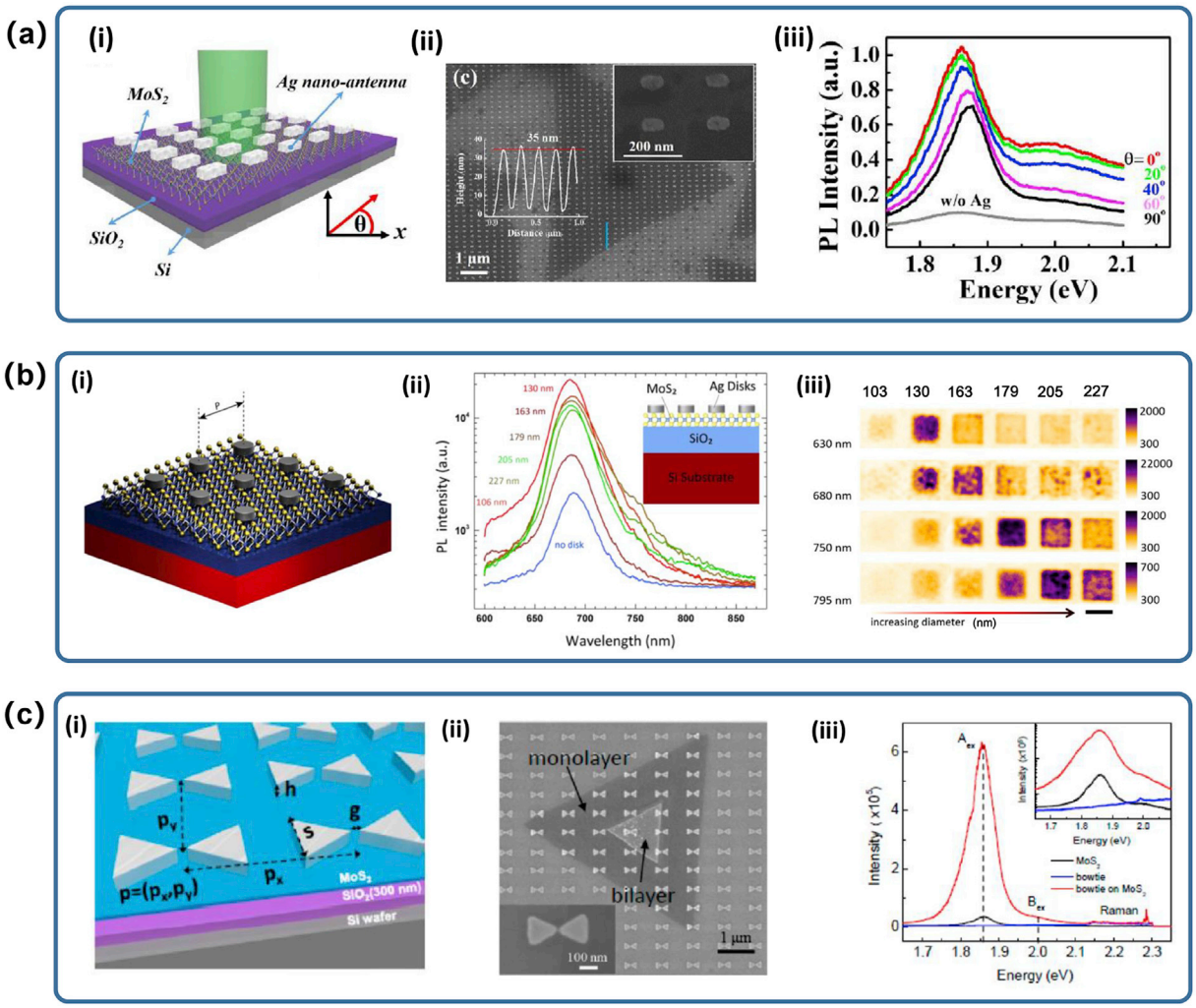

Fig. 6. Enhanced PL of hybrids formed by fabricating periodic NSs on top of TMDs (NSs/TMDs). (a) i: Scheme of periodic Ag nanoantenna arrays on monolayer MoS_2. ii: The SEM image of nano-antenna arrays on MoS_2. iii: PL spectra in Ag nano-antenna coated MoS_2 under excitation with different polarization angles θ, comparing with pristine monolayer MoS_2. Reproduced with permission [35]. Copyright 2016, Springer Nature. (b) i: Schematic representation of plasmonic nanodisc arrays/MoS_2 heterostructures. ii: PL intensity comparison of selected points in each array. Inset shows the cross-section of the heterostructure. iii: PL emission 2D spatial maps at four different wavelengths of six varying diameter nanodisc arrays. Scale bar is 25 μm. Reproduced with permission [83]. Copyright 2015, American Chemical Society. (c) i: Scheme of the bowtie arrays on monolayer MoS_2. ii: SEM image showing the silver bowtie array directly patterned on well-defined, stacked triangular flakes of mono- and bilayer MoS_2. The larger triangular flake of darker contrast corresponds to a single layer and the smaller flake of lighter contrast to a bilayer. iii: PL spectra of bare MoS_2, bowtie array and bowtie-MoS_2. Reproduced with permission [38]. Copyright 2015, American Chemical Society.

high-field region of the plasmonic mode generated on the hybrid of WSe_2 and nanopillars, as presented in Fig. 7(b)-i and 7(b)-ii [36]. Si nanopillars were fabricated by inductively coupled plasma (ICP) etched using template on Si substrate, followed with 10 nm thick gold layer and a 6 nm thick Al_2O_3 layer coated on top. Each nanopillar introduced a deformation in the atomically thin WSe_2 that covered it, leading to the generation of strain-induced single defects in close proximity to the plasmonic mode, as evidenced by the PL intensity map exhibited in Fig. 7(b)-iii. Compared with bare WSe_2, the full width at half-maximum (FWHM) of this emitter was much narrow, just about 0.55 nm. In addition to physical etching methods, an AAO template-based sputtering method was introduced by Yu et al. to fabricate the plamonic nanopillars/MoS_2 heterostructure [91]. An Al_2O_3 barrier layer was fabricated on the surface of Au nanoantenna film, and then the charge transfer from Au nanopillars into MoS_2 were studied utilize femtosecond pump-probe spectroscopy.

Besides the lift-off methods, physical etching on metal films are also a rout to fabricate plasmonic nanopatterns to support TMDs [92]. In 2016, Wang et al. reported a giant PL enhancement on the hybrid of WSe_2-nanotrenches [39]. As illustrated in Fig. 7(c)-i, CVD-grown WSe_2 monolayer flakes was transferred onto a gold substrate with nanotrenches. The width of nanotrenches was of ~12 nm as presented the SEM image in Fig. 7(c)-ii. As shown in Fig. 7(c)-iii, the maximum PL enhancement was achieved at WSe_2 on a nanostructure with the pitch of 200 nm. Under the 633-nm pump laser wavelength which is close to the gap plasmon resonance, the integrated PL intensity from WSe_2 on this gold nanostructure was enhanced up to 20000-fold (after correcting for the trench area fraction).

Apart from nanotrenches, nanohole arrays can be feasibly obtained by physical etching method, and have been introduced to boost the PL of MoS_2, as illustrated in Fig. 7(d)-i [37]. The nanohole arrays were fabricated using FIB on Ag film that was previously sputtered on Si substrate. Fig. 7(d)-ii exhibits the optical image of a MoS_2 triangular domain covering the Ag nanohole array with a period of 450 nm.

In addition to the hybrid nanosystems composed by transferring

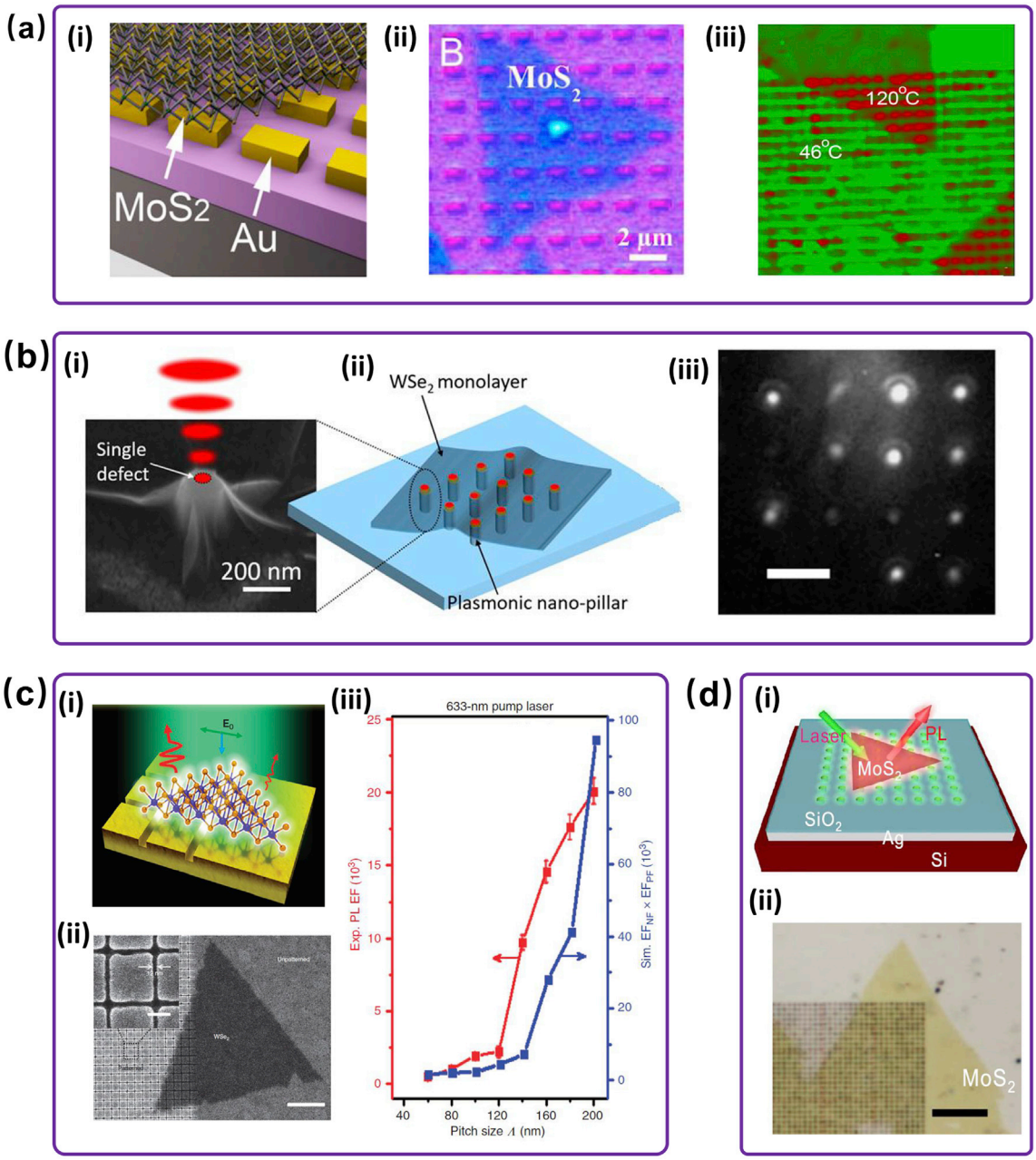

Fig. 7. Enhanced PL of plasmonic hybrids by placing TMDs on top of NSs previously fabricated on a substrate (TMDs/NSs). (a) i: Side view cartoon showing the general features of MoS_2-gold nanoantenna hybrid. ii: Top view optical microscopy image showing the region of MoS_2 coated and bare gold nanoantennas. iii: Temperature map obtained by converting the PL peak wavelengths to temperatures in °C. Reproduced with permission [34]. Copyright 2014, American Chemical Society. (b) i: Scheme of the hybrid of WSe_2 on nanopillars. ii: SEM image of a single plasmonic nanopillar covered by a WSe_2 monolayer. iii: Photoluminescence intensity map of arrays of plasmonic nanopillars covered by WSe_2 monolayer. Scale bar: 4 μm. Reproduced with permission [36]. Copyright 2018, American Chemical Society. (c) i: Schematic of PL emission from a single crystal monolayer of WSe_2 flake on a gold substrate. ii: SEM image of WSe_2 on square arrays with trenches. The scale bars in the main Fig. and the inset, 1 mm and 100 nm, respectively. iii: Experimental PL enhancement factor and the simulated $EF_{NF}XEF_{PF}$, respectively. Reproduced with permission [39]. Copyright 2016, Springer Nature. (d) i: Schematic view of a sample fabricated with MoS_2 flakes transferred onto the hole arrays in silver film. ii: Photograph image of the MoS_2 flakes placed on hole arrays. Reproduced with permission [37]. Copyright 2018, Optical Society of America.

TMDs on NSs, hybrids can also be achieved by directly growing TMDs on NSs [93,94]. Recently, a facile approach was proposed to successfully integrated few-layer MoS_2 on Au nanodiscs by sulfur driven segregation of Mo from a preformed Mo–Au alloy nanostructures [94].

3.1.5. Sandwich-like architectures (nanoscale metals/TMDs/mirror metal layer or periodic nanostructures)

Lastly, the enhanced PL properties of the three-layer sandwich-like hybrid heterostructures are discussed. Introducing an additional metal layer or nanostructures can form a nanocavity with existing NPs (or NSs), in which SPPs generate at the metal-TMDs interface, leading to the significantly enhancement of the PL emission of TMDs [95,96].

The represented works based on the three-layer sandwiched hybrids are shown in Fig. 8. Cheng and co-workers reported a Ag NW-WS_2-Ag film plasmonic system to enhance the PL emission, and systematically studied the effects of spacer and crystalline of Ag

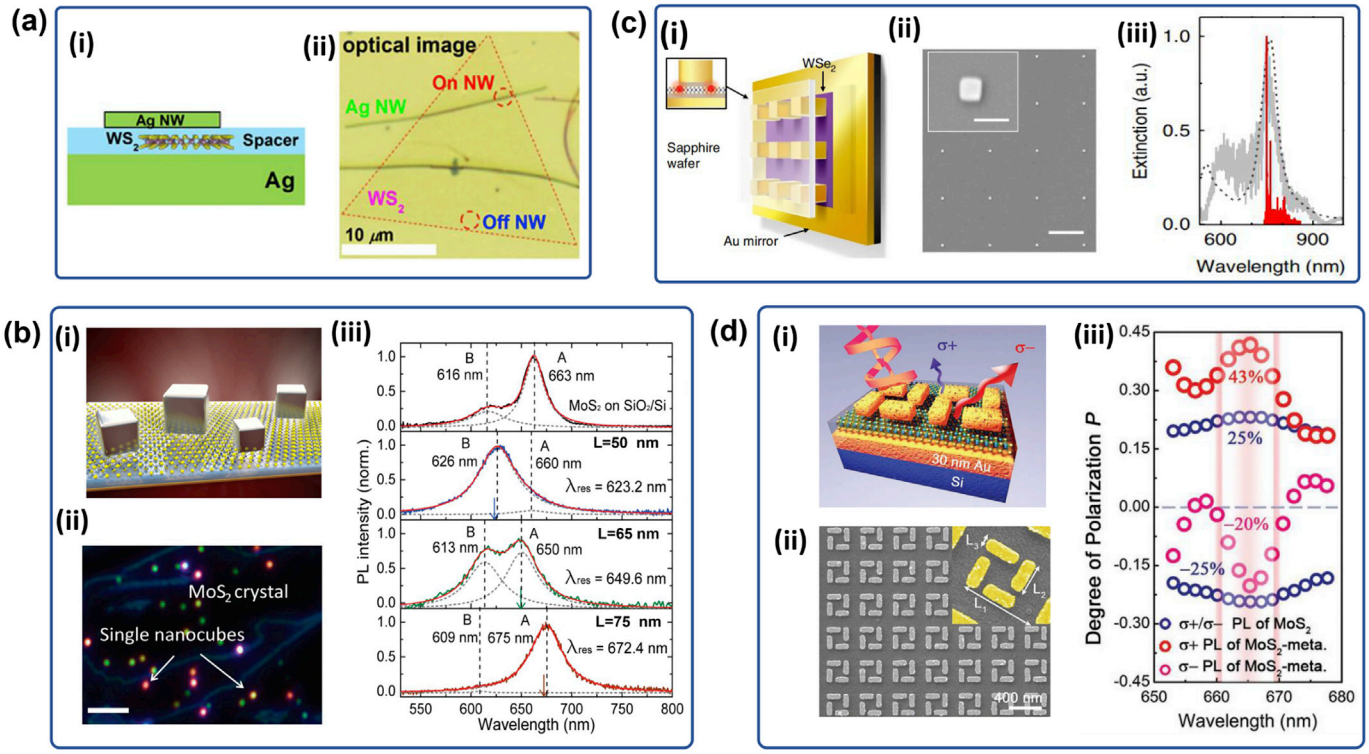

Fig. 8. Enhanced PL for the three-layer sandwich-like hybrids. (a) i: Schematics illustrating an WS_2 flake sandwiched between a Ag film and a Ag NW (d = 120 nm). 2 nm Al_2O_3 is inserted below and above the WS_2 flake. ii: Optical image of a NW-WS_2-film composite. Reproduced with permission [43]. Copyright 2017, American Chemical Society. (b) i: 3D illustration of the plasmonic nanocavity. ii: Dark-field microscope image of the fabricated sample. The scale bar is 5 μm iii: Shifted PL emission peaks relative to the control sample when monolayer MoS_2 is coupled to nanocavities with varying resonances. The plasmon resonance (λ_{res}) for each individual nanocavity is indicated by the arrow in each panel. Reproduced with permission [63]. Copyright 2017, American Chemical Society. (c) i: Schematic of monolayer WSe_2 coupled to a plasmonic Au nanocube cavity array. ii: SEM image of the Au nanocube array on a sapphire substrate. Scale bar, 2 μ m. Inset, Magnified view of an individual Au nanocube. Scale bar, 200 nm iii: Simulated (dashed line) and measured (grey solid line) plasmon resonance spectra together with the localized exciton spectrum (red solid line) of a typical quantum emitter directly induced by the Au nanocube into WSe_2. Reproduced with permission [44]. Copyright 2018, Springer Nature. (d) i: Schematic of MoS_2-metasurface structure, where CVD-grown MoS_2 monolayer is placed into the SiO_2 layer, and sandwiched between chiral metasurface and Au film. ii: SEM image of metasurface array. Inset is the SEM image of metasurface unit. Iii: Circularly polarized PL spectra of MoS_2 and MoS_2-metasurface. Reproduced with permission [101]. Copyright 2018, WILEY-VCH Verlag GmbH & Co.

mirror [43]. Fig. 8(a)-i illustrates a sectional view of the NW-WS_2-film composite. It is demonstrated that a 1–2 nm Al_2O_3 spacer can effectively prevent PL quenching of WS_2. As shown in Fig. 8(a)-ii, the optical image presents the relative position of the Ag NWs with respect to the WS_2 flake, and PL was collected on several specific locations. For the composite on an epitaxial Ag film, the PL on NW was ~2.1 times of that off NW.

Plasmonic nanocavities based on a film-coupled nanopatch antenna were designed to tailor the PL emission of MoS_2, in which a 1200-fold enhancement of the A exciton emission and a 6100-fold enhancement of the B exciton emission were detected [63]. As illustrated in Fig. 8(b)-i, the colloidally synthesized nanocubes have a range of sizes, from 50 to 75 nm, were deposited on the CVD-grown MoS_2 covered by a 1 nm polyelectrolyte adhesion layer. MoS_2 was transferred on the substrate covered with a 5 nm Al_2O_3 and 75 nm gold film on top of a Si substrate. As the dark-field scattering image exhibited in Fig. 8(b)-ii, the edges of MoS_2 monolayer appeared as the blue outlines and the individual nanocavity can be identified as a bright spot. The different colors of the spots represented the varying resonances of each film-coupled nanocube's associated fundamental cavity mode. As exhibited in Fig. 8(b)-iii, the peak emission wavelengths of the A and B excitons can be tuned up to 40 and 25 nm, while the average nanocube size of nanocubes increased from 50 to 75 nm. In recent years, shell-isolated nanoparticles (SHINs) have been demonstrated to be high performance in SERS [97]. After dispersing Ag SHINs on top of the monolayer MoS_2 transferred on Au film, a PL enhancement of 110-fold was achieved [98].

Dispersing plasmonic nanocubes randomly onto a substrate lacked spatial control and limited the coupling. Luo and co-workers demonstrated a deterministic approach to achieve high Purcell enhancement at lithographically defined locations using the sharp corners of a metal nanocube for both electric field enhancement and to deform a 2D material [44]. As illustrated in Fig. 8(c)-i, the WSe_2 was separated from the Au cubes and the planar Au layer by a 2 nm Al_2O_3 spacer layer on each side to prevent optical quenching and short-circuiting of the nanoplasmonic gap mode. Fig. 8(c)-ii displays the SEM of the Au nanocube array with 2.5 μ m pitch, in which the flat-top cubes were of a near-unity aspect ratio with a height of 90 nm and side length of 110 nm (see the inset). The broadband response of the plasmonic mode was tailored to coincide with the exciton emission wavelength (750–800 nm), as depicted in Fig. 8(c)-iii. Utilizing nanocube corners to form vertical plasmonic gap modes against a planar Au mirror, the PL was enhanced by 13 times. It is demonstrated on this kind of quantum emitters that the Purcell factors was up to 551 (average of 181), single-photon emission rates was up to 42 MHz and a narrow exciton linewidth was as low as 55 μeV.

Utilizing a coupled spin and valley degree of freedom, semiconducting TMDs show prominent application prospect of valleytronics devices. Polarization-resolved PL has been demonstrated to be a feasible tool to study and modulate the valleytronics property of TMDs [99,100]. A type of meta-dielectric-metal plasmonic chiral structure was developed by Li et al. to manipulate valley-polarized

PL in MoS_2-metasurface heterostructure [101]. As illustrated in Fig. 8(d)-i, valley-polarized PL of MoS_2 was tailored with near-field interaction under the excitation of specific circularly polarized light. Fig. 8(d)-ii shows the SEM image of metasurface fabricated using EBL. A metasurface unit is of the unit length L1, L2, and L3 of 400 nm, rod length of 190 nm, and rod width of 75 nm (see the inset). Fig. 8(d)-iii exhibits polarized PL detection of MoS_2 monolayer and MoS_2-metasurface under the excitation of left-handed circularly polarized light (LCP, σ−) at 87 K. The intensity of σ− PL for MoS_2-metasurface was significantly increased due to the enhancement of EM near-field, while the intensity of right-handed circularly polarized (RCP, σ+) PL was decreased accompanied by a change in the spectral shape. The above observations were attributed to the interaction between the excitons and the chiral near-field modes.

3.2. Enhanced reflectance and absorbance properties

Except the PL emission, other optical responds of TMDs, such as reflectance and absorbance, can also be modulated through the hybridization with plasmonic nanoscale metals, which are very important criteria for the light harvesting efficiency in photoelectric devices [38,82,102,103]. In addition, reflectance spectroscopy is a feasible tool to investigate the strong coupling between plasmons and excitons, because a week coupling occurs for most of plasmonic hybrid frameworks and can only enhance the PL emission. Fig. 9 presents several typical works based on plasmonic hybrid heterostructures with different architectures.

Strong coupling between plasmons and excitons in nanocavities gives rise to the formation of hybrid plexcitonic states, inspiring fundamental quantum science in nanoscale and potential applications in applications including optoelectronics [104–106]. Using a single silver nanorod as a Fabry-Pérot nanocavity, Zheng and co-workers realized strong coupling of plasmon in single nanocavity with excitons in a monolayer WSe_2 [64]. As illustrated in Fig. 9(a)-i, this plexciton system was fabricated by simply dropping cast and spinning a metal nanorod onto a mechanically exfoliated WSe_2 monolayer. Before depositing nanorods, an alumina layer of 3.2 nm was deposited onto the WSe_2 to prevent direct contact to the nanoparticle. Fig. 9(a)-iii and iv presents the dark-field scattering spectra of the silver nanorod on and off WSe_2 layer, respectively, as a function the thickness of alumina coating. One can see that the surface plasmon energy E_{pl} shifted across the exciton E_0 of WSe_2 clearly evidenced the strong coupling-spectral splitting in the scattering spectra. Moreover, the resonant peaks were slightly broader than those from bare nanorods because of the absorption in WSe_2.

When the hybrid plexcitonic states is produced, the wave

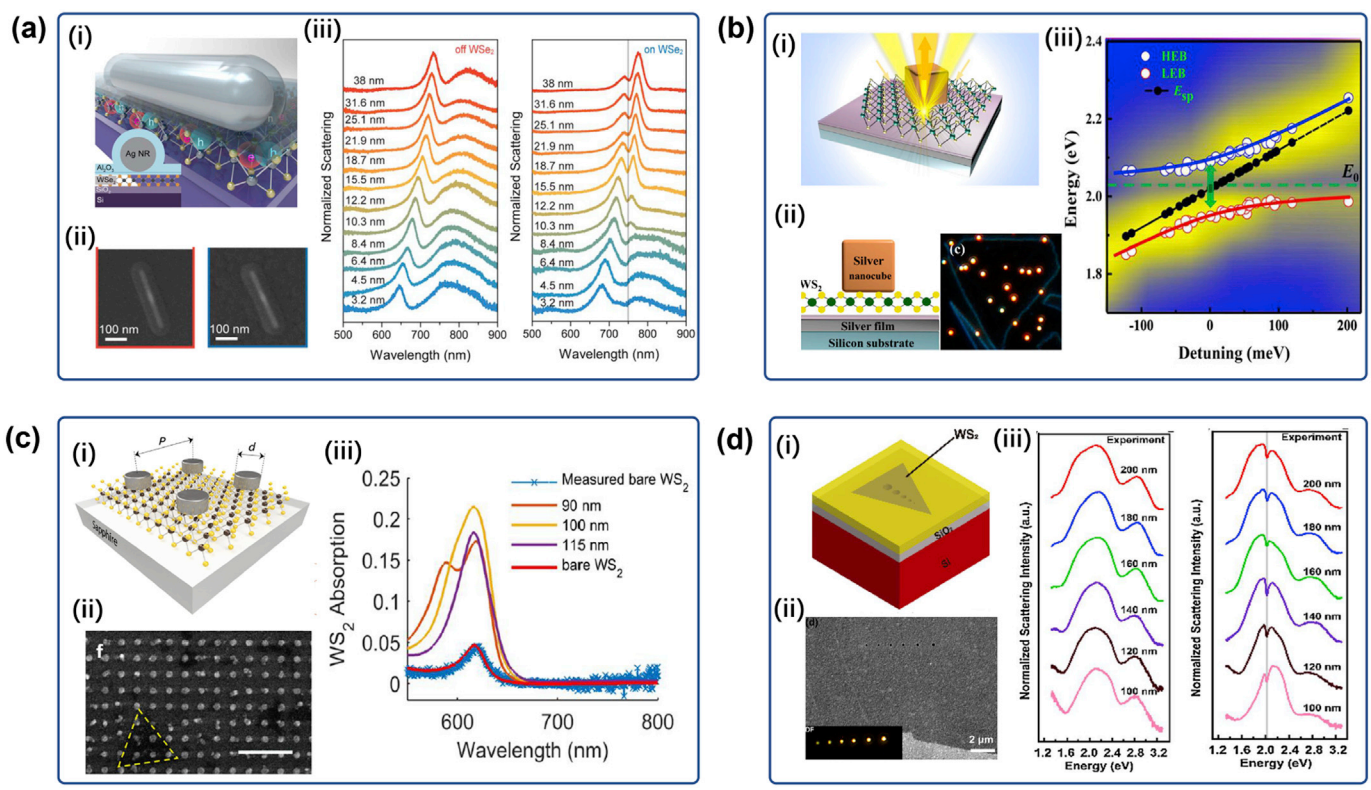

Fig. 9. Absorbance and reflectance properties of TMDs modulated by plasmonic hybrids. (a) i: A schematic of the system with a single silver nanorod on a monolayer WSe_2. ii: SEM image of the silver nanorod on bare substrate and a monolayer WSe_2. iii: A set of dark-field scattering spectra of the silver nanorod on bare substrate and on a monolayer WSe_2 with increased alumina coating. Reproduced with permission [64]. Copyright 2017, American Chemical Society. (b) i: Schematic experiment setup for measuring dark-field scattering signals of individual nanoparticles. ii: Cross-section diagram and dark-filed microscope image of the hybrid nanostructures. iii: Dispersion of plexciton with HEB and LEB varied as a function of detuning. Blue and red dots indicate experimental data extracted from scattering spectra. The solid lines are fits of the couple harmonic oscillator model. Black dots present the plasmon energy of the pure plasmonic nanocavity, while green dash line indicates the exciton resonance of WS_2 monolayers. Reproduced with permission [65]. Copyright 2018, American Chemical Society. (c) i: Conceptual schematic of the proposed WS_2/Ag plasmonic heterostructure on sapphire. ii: SEM image of one of the plasmonic arrays on WS_2. The scale bar is 1 μm iii: Spectral absorption comparison of Ag/WS_2 heterostructures as a function of nanodisk diameter. Reproduced with permission [110]. Copyright 2017, American Chemical Society. (d) i: Scheme of a hybrid gold nanonole−WS_2 nanostructure fabricating using FIB milling and van der Waals assembly procedure. ii: SEM image of the WS_2 on top of the gold NH array. The inset shows a dark-field scattering image of the WS_2 monolayer after being transferred onto the gold NH array. iii: Measured dark-field scattering spectra for the gold nanoholes (left panel) and monolayer WS_2/gold NH hybrid (right panel). Reproduced with permission [112]. Copyright 2019, Elsevier Ltd.

functions of the initial emitter and the electromagnetic mode in a cavity are coherent superpositions [107]. TMDs, as the emitter with high oscillator strength and a high exciton binding energy [108,109], exhibit the potential for studying strong coupling with larger Rabi splitting at higher temperatures. Han et al. proposed a plasmonic nanocavity based on a three-layer hybrid composed of Ag nanocubes, monolayer WS_2 and a silver layer, as illustrated in Fig. 9(b)-i, which can produce a large Rabi splitting at room temperature [65]. The hybrid plasmonic nanocavity was composed of individual silver nanocubes and a silver film. Monolayer WS_2 and a spacer film (Al_2O_3) were embedded in the gap, as shown in Fig. 9(b)-ii. As presented in the dark-field scattering image, the boundary of the WS_2 monolayer appeared a blue outline and monodispersed silver nanocubes were indicated by small bright spots. The surface plasmon resonance (SPR) of the nanocavity can be tuned by controlling the thickness of nanogap and the size of silver nanocubes, which allows to successively adjusting the SPR to accurately match the exciton energy of WS_2 monolayers. Splitting took place in the scattering spectra, in which the high and low energy branches (HEB and LEB) were fitted, as presented in Fig. 9(b)-iii. A large Rabi splitting of ~145 meV was obtained in the hybrid nanostructures, as indicated by the green arrow.

The periodic metal nanostructures are good candidates for fabricating plasmonic hybrid heterostructure because the resonance center can be tuned easily by adjusting the size, shape, and period of the nanostructures [110,111]. A TMDs/NSs hybrid heterostructure was developed by Butun et al. to study of the modulated absorption properties of WS_2 [110]. As illustrated in Fig. 9(c)-i, the hybrid heterostructure was composed of periodic nanodisks and a monolayer WS_2 on sapphire substrate. The contrast difference between the WS_2 film and the sapphire surface can be seen in the SEM image in Fig. 9(c)-ii. Fig. 9(c)-iii presents the FDTD simulations of hybrid heterostructure as a function of nanodisk diameter. An enhancement more than 4-fold was achieved in the absorption of WS_2 films for 100 nm diameter nanodisks. An asymmetric feature resembling Fano line shape appeared in the reflection spectra of the bowties-MoS_2 hybrid, which was attributed to the decreased damping of MoS_2 excitons interacting with the plasmonic resonances of the bowtie arrays at low temperatures [38].

In 2019, the resonance plasmon-exciton coupling was studied on a TMDs/NSs system by integrating monolayer WS_2 with an individual nanohole (NH), in which a Rabi splitting exceeding 162 meV was achieved at room temperature [112]. As shown in Fig. 9(d)-i, the NHs were fabricated using FIB on 10/100 nm Ti/Au film deposited a Si substrate. The size of the NH can be customized with the diameter varied between 50 and 300 nm, as shown in Fig. 9(d)-ii. The NH can exhibit strong light scattering intensity after capped with the momolayer WS_2 flake (see the inset in Fig. 9(d)-ii). Compared with bare NH, the scattering spectra of the hybrid WS_2/Au NH exhibited mode splitting, which was characterized by two broad resonances separated by a scattering dip, as shown in Fig. 9(d)-iii. Such a mode splitting behavior indicated the resonance coupling between the LSPR and WS_2 exciton to occur.

3.3. Enhanced Raman spectra

As we know, nanoscale metals have been widely employed in surface enhanced Raman spectroscopy (SERS) studies to detect the low concentrated analyte molecules absorbed on the surface of nanoscale metals. As a result, the enhancement of the intrinsic Raman spectra of TMDs were observed while study the enhanced optical properties of the TMDs-nanoscale metals hybrids [29,37,38,70,79]. In addition, some research work have specially focused on the SERS of TMDs due to the plasmonic hybridization [113,114], and the typical results have been summarized in Fig. 10.

It is well known that the detection sensitivity for SERS depends crucially on the size and shape of NPs. In 2016, Zhang et al. systematically studied the effect of the distribution of the metal NPs on the SERS of WS_2 and MoS_2 based on NPs/TMDs hybrids, as illustrated in Fig. 10(a)-i [115]. When the nominal thickness was increased from 1 nm to 10 nm, the morphology of Ag NPs was modified. As presented in Fig. 10(a)-ii, Ag NPs were separated but elongated and Ag NPs with multiple axes emerge for 5 nm thick Ag NPs. After growing Ag NPs on top of monolayer WS_2, an increase in the intensity of the Raman modes was clearly observed, as shown in Fig. 10(a)-iii. The intensity of 2LA(M) mode was enhanced by a factor of 3. The highest enhancement took place at the 5 nm thick Ag NPs.

Due to due to colloidal agglomeration of NPs produced by chemical recution method, it is difficult to control uniform size and distribution of NPs on the surface. Yang and co-workers developed a Ag/WS_2 hybrid structure by transferring monolayer WS_2 on large-area periodic Ag nanoprism array prepared using the nanosphere lithography (NSL) method [116]. As illustrated in Fig. 10(b)-i, a 50 nm thick Ag film was thermal evaporated on a monolayer of hexagonal closed package polystyrene nanospheres. After ultrasonic cleaning in ethanol, the upper metal film was lift-off, eventually leaving triangular Ag nanoprism arrays on the substrates. As the AFM image in Fig. 10(b)-ii displayed, the side length of Ag nanoprism was 85 nm. The Raman spectrum of the WS_2 on Ag nanoprisms was obviously enhanced, as presented in Fig. 10(b)-iii. The intensity enhancement factors for the E_{2g} and A_{1g} modes were 3 and 4, respectively.

Although the nanogap structure has been demonstrated the ability for plasmonic enhancement, quantitative probing the quantum-limited plasmonic enhancement in nanogap remains a challenge. In 2018, a sandwich-like hybrid of MoS_2 spaced nanoparticle-on-mirror (MoS_2-NPOM) system was proposed to measure the plasmonic enhancement in the gap by quantitative SERS [117]. As illustrated in Fig. 10(c)–i and 10(c)-ii, the gap distance of the MoS_2-NPOM was precisely tuned by the number of layers of the MoS_2 interlayer in intervals of 0.62 nm. The TEM images in Fig. 10(c)–ii clearly show a subnanometre gap in MoS_2-NPOM structure. Fig. 10(c)–iii displays the Raman spectra obtained from a 1L MoS_2 on quartz, a 1L MoS_2 on ultrasmooth gold film and a 1L MoS_2-NPOM with a 32-nm-thick Al_2O_3 surface coating. Both the A_{1g} and A'_{1g} modes were greatly enhanced in the MoS_2-NPOM, whereas the intensity of A_{1g} mode was approximately two orders of magnitude higher than that of A'_{1g} mode.

Besides regular Raman spectra of TMDs, chiral Raman signal can be also tuned by plasmoic nanoscale metals. Recently, the high-fidelity routing of a chiral Raman signal into propagating surface plasmon polaritons along a silver NW based on spin-orbit interaction of light was reported by Guo et al. [118]. As illustrated in Fig. 10(d)-i, the plasmonic hybrid was consisted of a single NW about 7.42 μm and multilayer WS_2. A circularly polarized (CP) laser with wavelength centered at 633 nm was focused on the WS_2 region near the NW. The incident photons undergo an inelastic Raman scattering process with retaining the CP states, which generated phonons in WS_2 and SPPs on the NW. As presented in Fig. 10(d)-ii, quantitative control over the Raman sorting was achieved by continuously rotating a quarter-wave plate (QWP). The position-dependent κ_{exp} reached a highly asymmetric and directional fashion (±0.4). This work extended the spin-orbit interaction of light to the Raman scattering regime and proposed a new perspective for the remote readout of local optical chirality, helicity-related directional sorting, and quantum information processing.

In addition to the plasmonic modulated Raman signal, hot

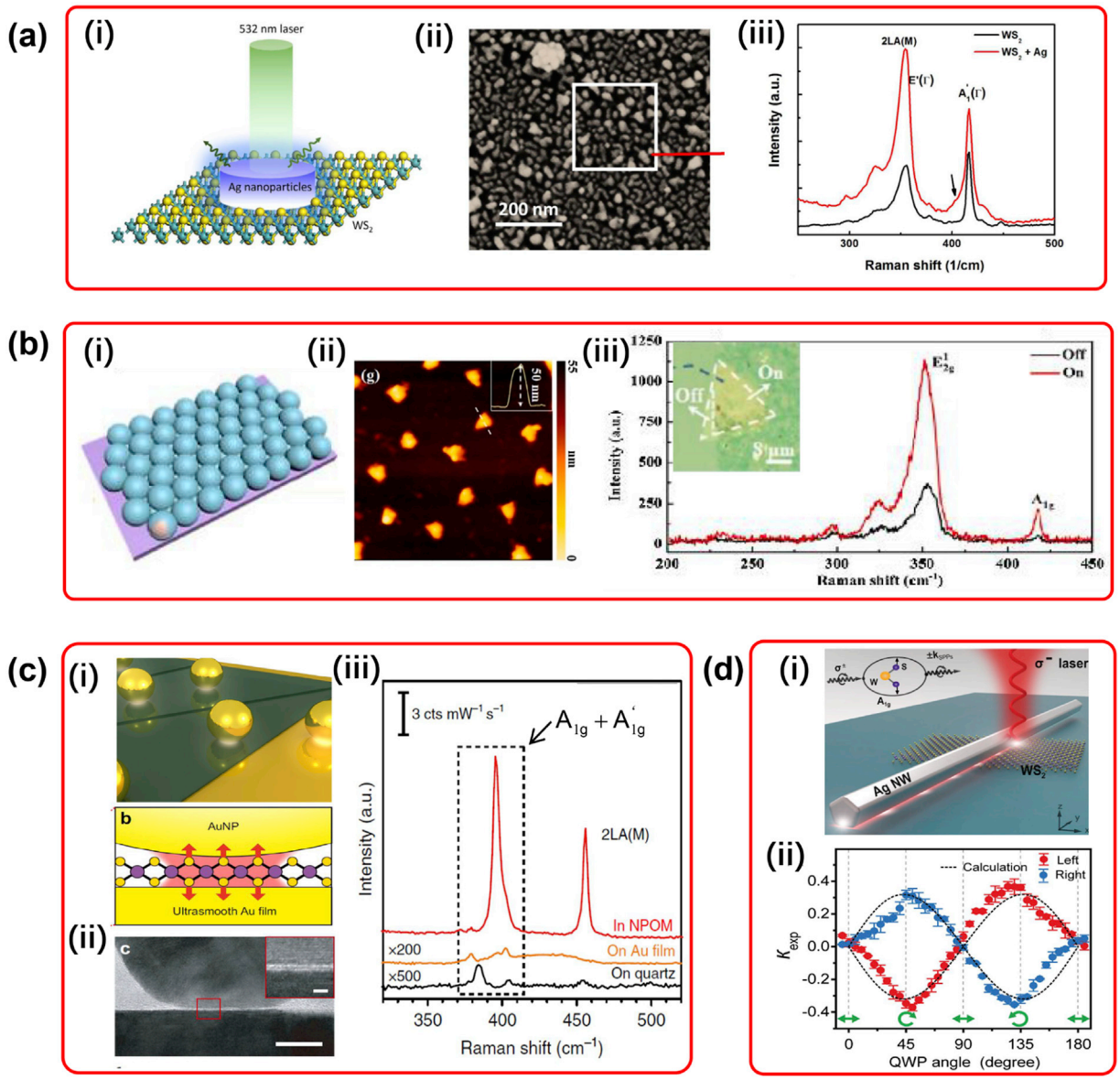

Fig. 10. Enhanced Raman scattering by plasmonic hybrids of TMDs-nanoscale metals. (a) i: Schematic drawing of the experimental setup for the SERS measurements of WS_2. ii: SEM image of 5 nm nominally thick Ag NPs on monolayer WS_2. iii: Raman spectra of monolayer WS_2 with and without 5 nm Ag NPs on top. Reproduced with permission [115]. Copyright 2016, Springer Nature Limited. (b) i: Schematic illustration of the fabrication process of Ag nanoprism array. ii: AFM picture of Ag nanoprism array. iii: Raman spectra of the monolayer WS_2 on and off the optimized Ag nanoprism array. The inset shows the optical image of as-transferred monolayer WS_2 onto the optimized Ag nanoprism array with a boundary. Reproduced with permission [116]. Copyright 2020, Elsevier B.V. (c) i: Schematic and ii: high-resolution TEM images of a 1L MoS_2-NPOM cross-section in its nanocavity region. iii: Raman scattering spectra of a 32-nm-thick Al_2O_3 coated 1L MoS_2-NPOM, a 1L MoS_2 on ultrasmooth gold film and on quartz, respectively. Reproduced with permission [117]. Copyright 2018, Springer Nature Limited. (d) i: Illustration of the configuration and mechanism of the plasmonic hybrid. CP incident photons (σ) undergo Raman scattering by WS_2. ii: Evolution plots of the directional coupling efficiency as a function of QWP. Reproduced with permission [118]. Copyright 2019, American Physical Society.

electron induced phase transition from 2H phase to 1T phase was observed in the hybrid of Au NPs/MoS_2 using Raman spectroscopy [119].

3.4. Nonlinear optical properties

TMDs have been demonstrated to offer extraordinary nonlinearity, and the researches on the application of the hybrids of TMDs-metasurface on the modulation of the nonlinearly optical properties of TMDs increased fast in recent years [120,121]. Photonic metasurfaces, a type of two-dimensional array of subwavelength-spaced optical nanoantenna, enable to tailor the electromagnetic response with unprecedented manipulation over the fundamental properties of light emission of TMDs, i.e. phase, amplitude, spin and polarization [122]. It is found that all the reported plasmonic hybrids used for studying the nonlinearly optical properties were based on the architecture of TMDs/NSs. Chen and co-workers presented a new type of nonlinear hybrid metasurfaces for the visible region, which consists of a single layer WS_2 and a phased gold nanohole array [123]. The magnitude of second-harmonic generation (SHG) was enhanced at least 2 orders.

A hybrid nanostructure constituted by transferring a monolayer WS_2 on the Au metasurface was proposed by Hu et al. which enhanced and manipulated the nonlinear valley-locked chiral emission of WS_2 at room temperature [124]. As presented in Fig. 11(a)-i, single-layer WS_2 sited on top of a Au metasurface.

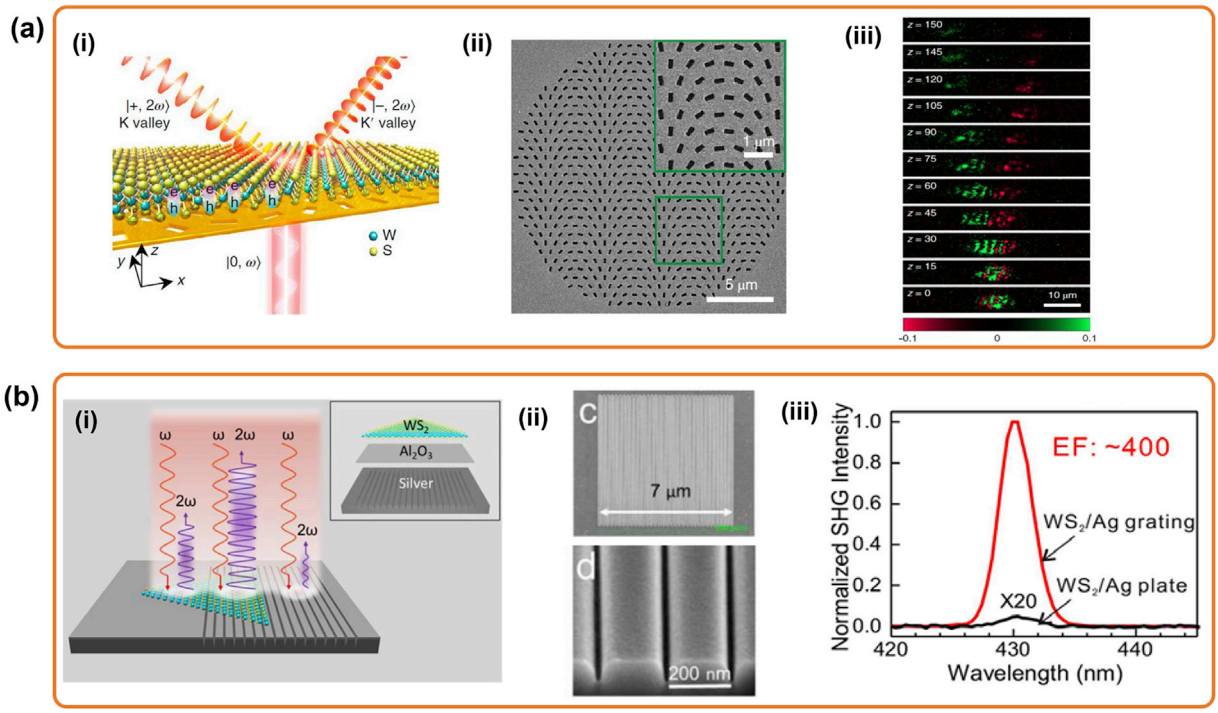

Fig. 11. Enhanced nonlinearly optical properties of TMDs by plasmonic hybrids. (a) i: Schematic of the synthetic Au–WS_2 metasurface. ii: SEM image of the photonic spin-Hall metasurface. iii: The experimentally measured differential energy distribution (ΔI, the difference between the RCP intensity, IRCP, and the LCP intensity, ILCP) and evolution of the second-harmonic signal along the propagation direction (z, in μm), which is normalized by the maximum measured total intensity in the z = 0 plane. Reproduced with permission [124]. Copyright 2019, Springer Nature. (b) i: Schematic diagram of the WS_2–plasmonic metasurface hybrid structure. The inset indicates the schematic of layered hybrid structure. ii: SEM image of the Ag nanogroove grating (Top panel). High-resolution SEM image showing the pitch and lateral profile of V-shaped nanogrooves in the grating (Bottom panel). iii: An EF of 400 can be determined from the SHG intensity ratio measured for patterned (nanogroove grating) and unpatterned regions covered by the same WS_2 flake. Reproduced with permission [125]. Copyright 2018, WILEY-VCH Verlag GmbH & Co.

Following the introduction of incident linearly polarized light (|0, ω>), the synthetic structure can yield large SHG from the valley band of the WS_2 and split opposite spin components of the second-harmonic valley photons (|+, 2ω> and |−, 2ω>) into different directions. Arrays of rectangular nanoholes arranged in a hexagonal lattice were fabricated by using FIB milling, as exhibited in Fig. 11(a)-ii. The plasmonic metasurface can enhance the nonlinear process responsible for SHG owing to the large plasmonic field localization around the nanoholes. The Au metasurface imposed a chirality-dependent Pancharantnam–Berry phase gradient, which arises from the photonic spin–orbit interaction, to the fundamental-frequency light. This gradient pumped the coherent SHG process and, consequently, steered nonlinear chiral photons emitted from different valleys in different spatial directions, as presented in Fig. 11(a)-iii.

In 2018, a dramatic enhancement (~400) of the SHG emission was achieved from monolayer WS_2 incorporated onto a 2D Ag nanogroove grating with subwavelength pitch [125]. Fig. 11(b)-i presents the schematic drawing of the WS_2-plasmonic hybrid metasurface structure for 2D plasmonic enhancement and manipulation of optical nonlinearity in monolayer WS_2. 60 nm-width V-shaped nanogrooves were milled by using a FIB on single-crystalline Ag plates synthesized on an indium tin oxide (ITO)-coated glass substrate. Fig. 11(b)-ii presents the SEM images of the obtained Ag nanogrooves. As exhibited in Fig. 11(b)-iii, a weak SHG signal was observed on the Ag grating structure, whereas the SHG intensity was greatly enhanced by 400 times for the hybrid WS_2–Ag nanogrooves.

Except noble metal nanostructures, other metal nanostructures were attempted to be employed in SHG. Recently, Guo et al. proposed a hybrid structure composed of monolayer WS_2 and aluminum (Al) plasmonic vortex metalens for chiral second-harmonic generation [126]. The enhanced chiral SHG conversion efficiency was designed at the C-exciton, which originates from the plasmonic vortex field-enhanced SHG under the optical spin–orbit interaction.

4. Devices applications based on plasmonic hybrids

Due to the extraordinary enhanced optical properties of the TMDs-nanoscale metals hybrid nanosystems, the potential applications are of growing interest in many fields as highly compacted light emitting devices, photodetectors in the visible and NIR range, THz devices and photocatalysis devices.

4.1. Photodetector in the visible range

Most of TMDs-based photodetector are employed for the visible light range due to the electronic bandgap energy of TMDs lying in the range of 1–2 eV. A photodetector based on TMDs/NPs hybrid consisting of a 1L-MoS_2 on top of Ag NW network, onto a transparent glass substrate, was developed by Bang and co-workers, as shown in Fig. 12(a)-i [76]. The long Ag NW (>35 μm) of an average diameter of 35 nm were synthesized by reduction methods. Fig. 12(a)-ii shows a dark field image of a hybrid photodetector fabricated using a 1L MoS_2 with Ag NW density of 60%. By hybridizing 1L-MoS_2 on Ag NW network, the overall photocurrent of photodetector was observed to be 250 times better than that of the pristine 1L-MoS_2 photodetector, as demonstrated by Fig. 12(a)-iii. In addition, the photoresponsivity and photodetectivity of the hybrid photodetector were effectively improved by a factor of ~1000.

Except the hybrids fabricated using the NPs synthesized using

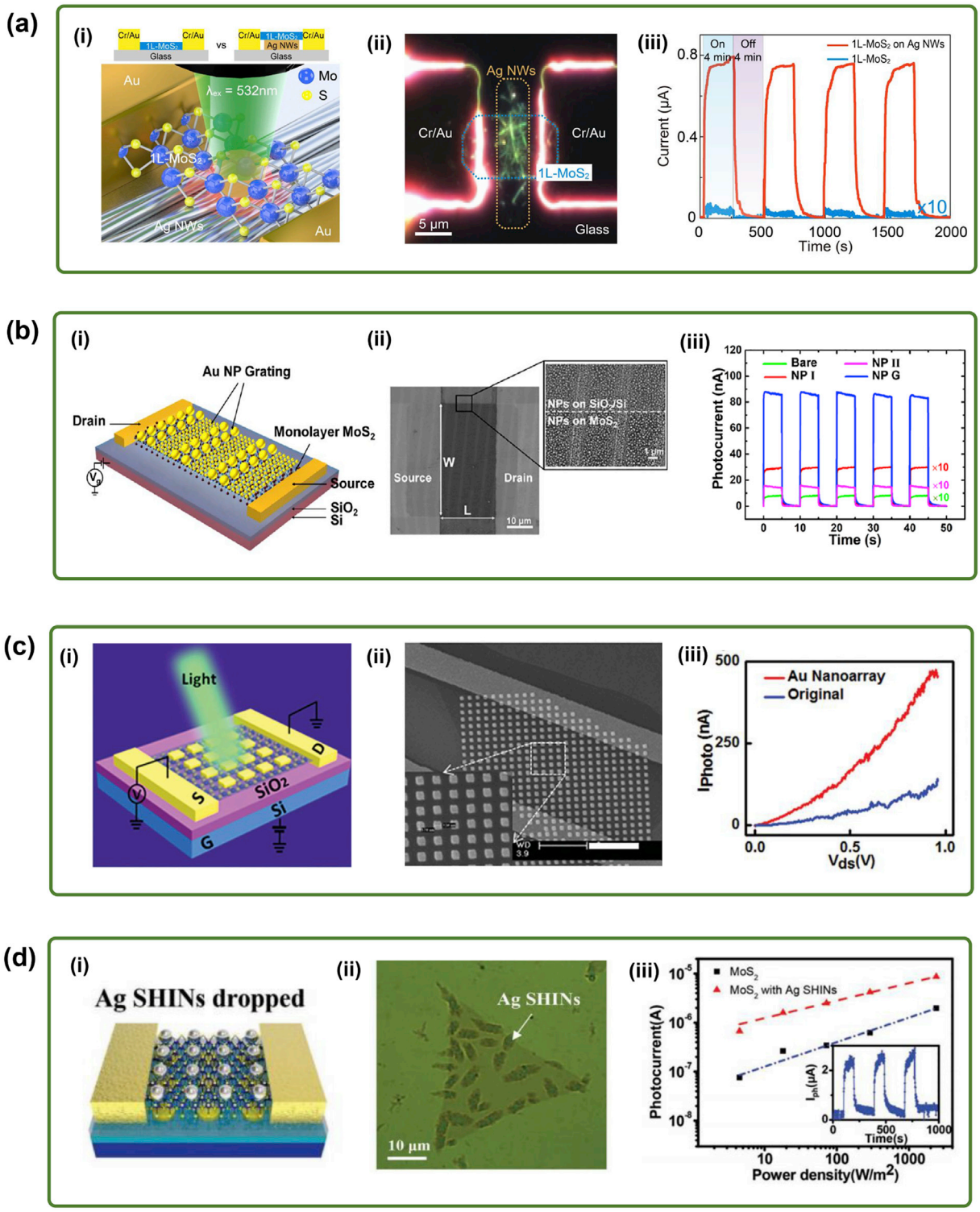

Fig. 12. Photodetectors in the visible range based on hybrids of TMDs-nanoscale metals. (a) i: Schematic diagram of device configuration of the hybrid photodetector. Upper diagrams are a simple schematic view of the pristine 1L-MoS_2 and the hybrid photodetector on a glass substrate. ii: Dark field image of the hybrid photodetector. iii: Time dependent photocurrent of the pristine 1L-MoS_2 (blue) and hybrid photodetectors (red) (on/off time = 4 min). Reproduced with permission [76]. Copyright 2018, American Chemical Society. (b) i: Schematic view of the nanoparticle grating/MoS_2 hybrid photodetector. ii: SEM images of the monolayer MoS_2 photodetector combined with nanoparticle grating. The width (W) and length (L) of the patterned MoS_2 is 80 and 40 μm, respectively. The inset is an amplified image of nanoparticles covering the Si/SiO_2 substrate and MoS_2. iii: Photocurrent–time response of the monolayer MoS_2 photodetector, the one with Nanoparticle I and nanoparticle grating. Reproduced with permission [129]. Copyright 2020, American Chemical Society. (c) i: Schematic of few-layer MoS_2 phototransistor with periodic Au nanoarrays. ii: SEM image of a typical few-layer MoS_2 phototransistor with 1 nm HfO_2 passivation layer and periodic Au nanoarrays. The scale bar is 2 μm iii: I_{Photo} versus V_{ds} output characteristics of the same phototransistor. Reproduced with permission [130]. Copyright 2015, Wiley-VCH Verlag GmbH & Co. (d) i: Schematic drawing for a MoS_2 photodetector. ii: Optical image of the same MoS_2 flake with Ag SHINs iii: Power-density-dependent photocurrent of a MoS_2 photodetector before and after dropping the Ag SHINs. Inset: The time response of a gap-mode plasmon-enhanced MoS_2 photodetector. Reproduced with permission [98]. Copyright 2018, WILEY-VCH Verlag GmbH & Co.

chemical methods on top of TMDs [127,128], directly depositing NPs on top of TMDs using physical methods were also adopted in the application on photodetector [70,129,130]. In 2020, Li et al. developed a NPs/TMDs photodetector incorporated monolayer MoS_2 with a grating-patterned nanoparticle structure that was fabricated using traditional photolithography together with an annealing step [129]. Briefly, a 5 nm thick Au grating was first fabricated through a lift-off process, and a second Au film with the same thickness was subsequently deposited to form a grating with alternating thicknesses (5 nm/10 nm). After annealing the film at 700 °C for 60 min, a grating shaped nanostructure assembled with the Nanoparticle I and Nanoparticle II was acquired. Then the obtained nanoparticles were transferred onto MoS_2, and the D/G sources are fabricated on the hybrid for device, as expressed in Fig. 12(b)-i. Fig. 12(b)-ii presents the SEM images of the Au nanoparticle grating/MoS_2 hybrid, in which the nanoparticle grating firmly stuck onto the underneath MoS_2 and SiO_2 films in the enlarged view. The current−time responses of the four types of photodetectors, namely, bare MoS_2 and MoS_2 with Nanoparticle I, Nanoparticle II, and nanoparticle grating, were measured under a 532 nm illumination. As shown in Fig. 12(b)-iii, the photocurrent for the nanoparticle grating-based devices increase is nearly 30 times larger than that of the devices with Nanoparticle I coatings and 111 times of bare MoS_2.

To evaluate the plasmonic enhancement on the photocurrent response between NPs and NSs, the few-layer MoS_2 phototransistor integrated with periodic Au nanoarrays was fabricated and compared with that decorated with Au nanoparticles [130]. As illustrated in Fig. 12(c)-i, the S/D electrodes and periodic Au nanoarray are defined by EBL, metallization, and lift-off processes. As exhibited Fig. 12(c)-ii, the Au nanoarrays deposited onto the MoS_2 phototransistor were quite uniform. The inset of Fig. 12(c)-ii shows the well-defined Au nanoarrays with 160 nm width, 180 nm length, 50 nm height, and 300 nm period. The MoS_2 phototransistor with Au nanoarrays has an overall 3 times higher photocurrent than those without Au nanoarrays, as shown in Fig. 12(c)-iii. In contrast, a just twofold increase was obtained on the MoS_2 phototransistor deposited with 4 nm thick Au nanoparticles.

Remarkably, a three-layer sandwiched hybrid system was also employed in photodetector base on a gap-mode plasmon-enhanced monolayer MoS_2 device integrated with Ag SHINs [98]. As illustrated in Fig. 12(d)-i, the Cr/Au circular array with a diameter of 5 μm and a spacing of 5 μm was firstly prepared on SiO_2/Si substrate by standard photolithography and the lift-off process. Then, CVD-grown h-BN and MoS_2 were transferred on the Au patterns, followed with deposition of Ag electrodes onto MoS_2. Finally, Ag SHINs with a diameter of 80 nm were dropped onto the MoS_2. In the optical image shown in Fig. 12(d)-ii, one can see that the Ag SHINs aggregated on MoS_2 rather than dispered on it . The power dependence of the photocurrent is displayed in Fig. 12(d)-iii. The photocurrent of the photodetector increases dramatically after dropping Ag SHINs. Specifically, the photocurrent can be increased by 882% (from 76 to 670 nA at 10 V) at the incident power density of 4.66 W m^{-2}, and the photoresponse can be improved from 32.6 to 287.5 A W^{-1}.

4.2. Photodetector in the NIR range

Except the photodetector applied in the visible range, TMDs have been extended to the near infrared range by the hybridization with nanoscale metals [131−133]. Different from the visible photodetectors, the plasmonic hybrid nanosystems applied in NIR photodetectors are in double-layer architecture.

Due to the limitation of the intrinsic bandgap of semiconductors, individual WS_2 and MoS_2 have no response to infrared light. Wang and co-workers developed an NIR light (1030 nm) photodetectors fabricated based WS_2/MoS_2 heterostructures, of which the responsivity was significantly enhanced by integrating with Au NPs [133]. As illustrated in Fig. 13(a)-i, after covered with Au NPs, the photodetector have high optoelectrical respond in visible-NIR range. The few layers WS_2/MoS_2 heterostructures were fabricated via mechanical exfoliation and target-transfer techniques. 22 nm Au NPs were synthesized using AAO template and then transferred onto the surface of WS_2/MoS_2 devices by wet transfer method. As shown in the SEM image of Au NPs decorated WS_2/MoS_2 heterostructure photodetector (see Fig. 13(a)-ii), the Au NPs has been uniformly dispersed on heterostructures surface. Fig. 13(a)-iii showed the on/off cycle test under 1030 nm light before and after Au NPs covering. The responsivity was enhanced by 25 times, suggesting a promising future application for high-performance infrared light photodetection.

By tuning the plasmonic nanostructures, the optoelectronic properties of 2D TMDs can be enhanced even beyond the bandgap of TMDs. In 2019, a broad spectral range (UV-visible-NIR) photodetector was integrated by fabricating Pt nanostrips on bilayer MoS_2, as presented in Fig. 13(b)-i [131]. The MoS_2 was transferred onto the SiO_2/Si substrate by using scotch tape method. Then, the source and drain electrical contacts, followed with the deposition of Pt nanostrips of width 590 nm and height 60 nm were deposited using FIB. Fig. 13(b)-ii presents the SEM image of the obtained plasmonic device. The detection sensitivity towards incoming NIR 980 nm laser light is shown in Fig. 13(b)-iii. The sudden increase and decrease in photocurrent, as shown by the arrows, indicate the switching on/off of the NIR light. A linear increase in the magnitude of the photocurrent rise as a function of laser light density was observed as shown in the inset. What is more, this device has been demonstrated a sensitivity to UV and visible light.

Utilizing a TMDs/NSs hybrid architecture, it was demonstrated that a sub-bandgap photocurrent can originate from the injection of hot electrons into MoS_2 as well as photo-amplification that yields a photogain of 10^5 [54]. As presented in Fig. 13(c)-i, the nonresonant wires (NRWs, color coded with green) are narrow such that the resonance modes are outside the wavelength range of the measurement, while the resonant wires (RWs, color coded with yellow) have antennas with a dipolar resonance at 1250 nm when illuminated with the electric field oriented along the y-direction. Au structures were first defined on a cleaned quartz substrate using EBL and deposition of 2 nm Ti and 15 nm Au films. ME bilayer MoS_2 was then transferred on top of the Au structures using a stamping method. Fig. 13(c)-ii presents the obtained hybrid MoS_2 NIR photodetector. The change of photoresponsivity as a function of source−drain voltage V_{sd} under illumination with a 150 nW E_y polarized 1070 nm laser is presented in Fig. 13(c)-iii. The measurements show increasing responsivity with increasing V_{sd} and a peak responsivity of 4.5A/W at 3 V bias, which is far above similar silicon-based hot electron photodetectors in which no photo-amplification is present.

4.3. THz devices

Graphene has been demonstrated as a good candidate for the room temperature THz devices because of its gapless band structure and high carrier mobility [134]. In contrast, TMDs are rarely employed in THz devices due to their optical bandgap in the range from UV to NIR. Although the ultrafast response time of photoconductivity (~ps) leads to great potential for highspeed THz devices [135], very few TMDs based THz devices were reported. So far, the reported hybrid THz devices are fabricated based on the TMDs/metasurface architecture.

An all-optical switching and modulation of micrometer scale

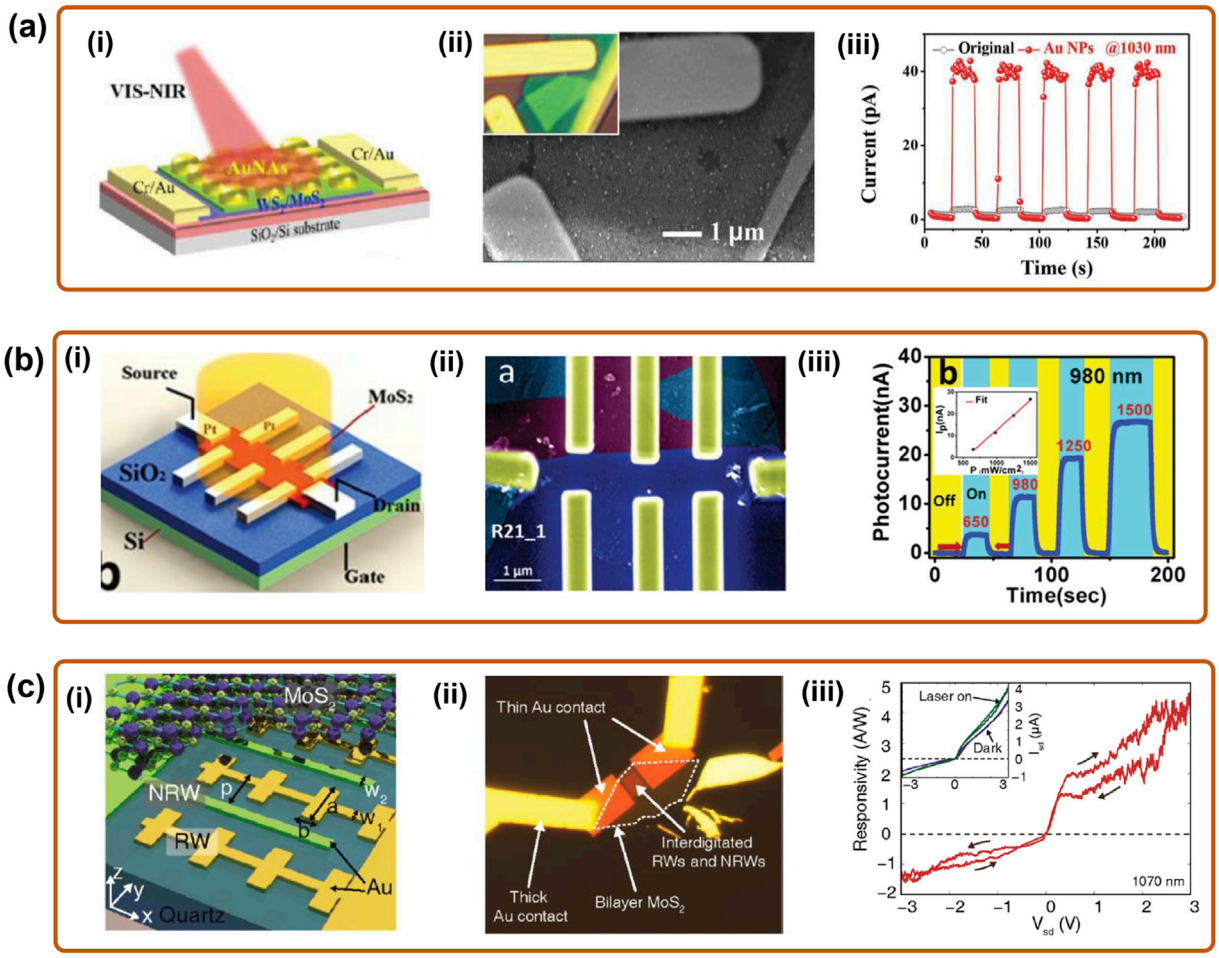

Fig. 13. Photodetectors in the NIR range based on hybrids of TMDs-nanoscale metals. (a) i: Schematic of photodetector covered with Au NPs pattern. ii: SEM image of heterostructures based photodetector covered with Au NPs pattern, inset shows the corresponding optical image of photodetector. iii: Comparison of on/off cycle stability test with and without Au NPs under 1030 nm light. Reproduced with permission [133]. Copyright 2018, WILEY-VCH Verlag GmbH & Co. (b) i: Schematic of the Pt nantostrips/MoS_2 device. ii: False-color image of the MoS_2 device after deposition of Pt nanostrips iii: Time-dependent photocurrent measurements under exposure to different NIR light intensities. The inset is the linear fit relation of the measured photocurrent and the incident laser power. Reproduced with permission [131]. Copyright 2017, WILEY-VCH Verlag GmbH & Co. (c) i: Schematic of the asymmetric plasmonic device. ii: Microscope image of the device with bilayer MoS_2 on top of the thin Au structures. iii: Photoresponsivity as a function of source–drain voltage (V_{sd}) measured at 1070 nm under E_y polarization. The inset shows the source–drain current (I_{sd}) as a function of V_{sd} under illumination and in a dark environment. Reproduced with permission [54]. Copyright 2015, American Chemical Society.

sub-wavelength Fano resonator was developed by Srivastava et al. [136]. Fig. 14(a)-i shows the graphical representation of the MoS_2-coated terahertz symmetric split ring (TASR) metamaterial sample illuminate by a terahertz probe beam and femtosecond optical pump beam. The TASR metamaterial was fabricated sing the photolithography process on quartz substrate. MoS_2 film was coated on the metamaterial using drop casting technique, as presented in Fig. 14(a)-ii. The transient dynamics of MoS_2 were studied for different pump fluences ranging from 63.5 μJ cm^{-2} to 254 μJ cm^{-2}. As shown in Fig. 14(a)-iii, a lifetime of the timescale of hundred picoseconds was achieved at moderate excitation pump fluences, implying the application in ultrafast switching resonator.

In 2020, Hu and co-workers proposed a type of ultrafast optical modulators composed of CVD-grown WSe_2 multilayer and plasmon-induced transparency (PIT) metasurfaces, which achieved the transmission amplitude modulation as high as 43% and the slow light switching up to 6 ps in the THz regime [137]. Fig. 14(b)-i illustrates the schematic architecture of the WSe_2/metasurfaces hybrid THz device. An array of coupled resonators between symmetry breaking split ring resonators SRRs and CRRs were adopted to realize to PIT resonance when excited by the incident THz wave. The passive metasurface generates the PIT window with enhanced sensitivity of external perturbations, and the top-covered WSe_2 layers acted as a photo-active medium to realize ultrafast modulation speed. The arrays of PIT structures were fabricated using standard UV photolithography on a z-cut silica substrate. A large-scale CVD grown WSe_2 multilayer directly adheres to the PIT metasurface layer with the aid of a wet transfer method. The hybrid structure of multilayer WSe_2-metasurface was exhibited in Fig. 14(b)-ii. If the device could be employed in the aspect of ultrafast slow light switches, the group delay of the metasurface can be actively modulated at an ultrafast speed. As presented in Fig. 14(b)-iii, the group delay modulation of the device exhibited an ultrafast switching speed within 8 ps.

4.4. Photocatalysis device

In addition to the optoelectronic devices, the plasmonic hybrids have been widely employed in photocatalysis. From the viewpoint of applications, the solution-processed hybrid of NPs/2D materials have been widely used in plasmon-enhanced photocatalytic reactions due to the large specific surface area. In recent years, some

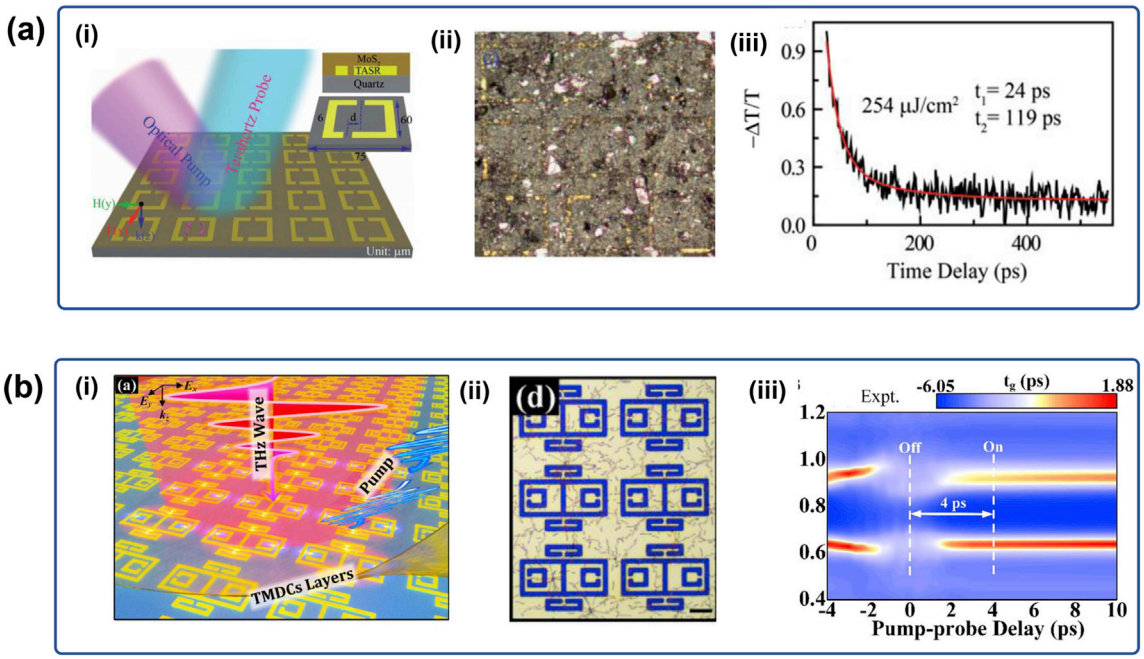

Fig. 14. THz devices in the visible range based on hybrids of TMDs-nanoscale metals. (a) i: An artistic illustration of the MoS_2 drop casted on MoS_2-TASR hybrid under the illumination of the optical pump and THz probe pulses. ii: Optical microscopy images of the TASR samples with drop-casted MoS_2 layer. iii: Experimentally measured photo-carrier relaxation dynamics (black line) of the drop-casted MoS_2 film on a quartz substrate performed using the OPTP measurements at excitation pump fluence 254 μJ cm^{-2} along with the corresponding biexponential decay fitting (red line). Reproduced with permission [136]. Copyright 2017, WILEY-VCH Verlag GmbH & Co. (b) i: An artistic illustration of the 2D TMDCs-covered PIT metasurface under femtosecond optical pumps. ii: Optical image of the hybrid metasurface covered by a WSe_2 multilayer with 40 nm thickness. Scale bar, 20 μm iii: Experimental measured group-delay spectra map of the metasurface against pump-probe time delay. The pump fluence was fixed at 800 μJ cm^{-2}. Reproduced with permission [137]. Copyright 2019, Elsevier Ltd.

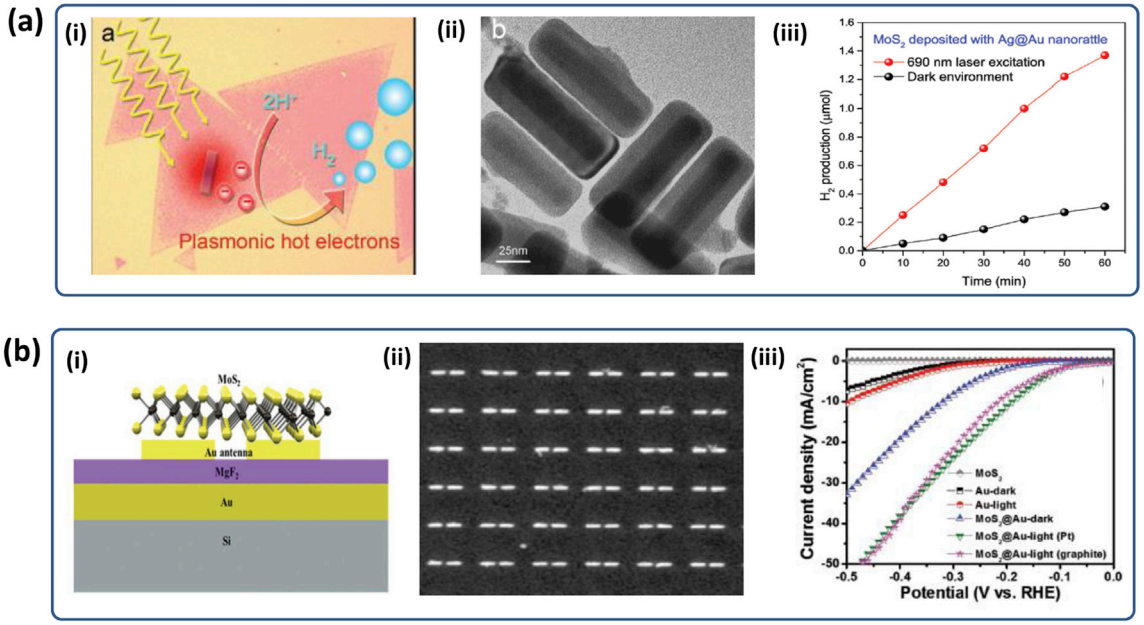

Fig. 15. Photocatalysis devices based on hybrids of TMDs-nanoscale metals. (a) i: Illustration of hot electron assisted MoS_2 catalysis in HER. ii: TEM image of Ag@Au nanorattles. The diameter and the length of the Ag core are about 20 and 80 nm, respectively, and the thickness of the Au shell is 10 nm iii: H_2 production as a function of time for the MoS_2 monolayers deposited with Ag@Au nanorattles under 690 nm laser excitation and in the dark environment. The H_2 gas was measured by gas chromatography, and the cell was purged with argon before the operation. Reproduced with permission [58]. Copyright 2015, the Royal Society of Chemistry. (b) i: schematic cross-sectional view of the QGP structure; ii: SEM image for the Taguchi-optimized QGP structure iii: HER polarization curves of Au, MoS_2, and MoS_2@Au with and without illumination recorded at the scan rate of 5 mV s^{-1} in 0.5 m H_2SO_4. Reproduced with permission [96]. Copyright 2018, WILEY-VCH Verlag GmbH & Co.

researchers have proposed the plenary hybrids of nanoscale metals/TMDs for the application in photocatalysis devices because of the strong plasmon-exciton coupling induced by the LSPR generated on nanoscale metals.

Owing to plasmonic induced hot electron doping, the CVD-grown monolayer MoS_2 with deposited Au@Ag nanorattles effectively enhanced the hydrogen evolution reaction (HER) efficiency [58]. The mechanism of plasmon-enhanced MoS_2 photocatalysis is illustrated in Fig. 15(a)-i. Plasmonic hot electrons generated from the Au-coated Ag (Ag@Au) nanorattles decorated MoS_2 monolayer. The 2H-to-1T phase transition makes the MoS_2 catalytic HER property dramatically improved and results in the effective production of hydrogen (H_2). The nanorattles with a core/shell structure are clearly shown in Fig. 15(a)-ii. The Ag core was 20 nm in diameter and 80 nm in length, and the thickness of the Au shell was about 10 nm. With 690 nm laser illumination, the device continuously produced H_2, which was about 1.35 μmol/h and much higher than the 0.3 μmol/h for the same experimental conditions but without laser excitation, as shown in Fig. 15(a)-iii.

A type of quadrupole gap plasmons (QGPs) using sandwich-liked architecture was proposed and applied in HER due to its accelerated electron injection process which is faster than the electron−hole pair recombination [96]. The optimized QGP structures were fabricated by the EBL process. Then, chemical vapor reaction (CVR)-grown bilayer MoS_2 was transferred to the QGP substrate via the soft-liftoff transfer process. As illustrated in Fig. 15(b)-i, a distinct nanogap was present between the antenna and the reflective mirror layer by depositing a 20 nm MgF_2 film, which experiences multiple reflections from the antenna terminations, forming GSPs, and resulting in a strong field enhancement. The SEM image shows the uniformly fabricated dipole antenna array (Fig. 15(b)-ii). The photocatalytic behavior of different samples toward the HER with and without light illumination was presented in Fig. 15(b)-iii. In contrast to bare bilayer MoS_2, MoS_2@Au-QGP structures exhibit enhanced HER activities with negligible variation in performance for Pt and graphite as counter electrodes.

5. Conclusion and outlook

In this review, we have addressed the architecture, mechanisms, enhanced optical properties and application device variants of TMDs-nanoscale metals hybrid nanosystems. As the light absorption of monolayer TMDs are lower than 10%, the main aim of the plamonic hybridization process is to enhance the ability of light harvest. Taking advantage of the sophisticated chemical synthesis methods and advanced nanofabrication techniques, plasmonic hybrid frameworks composed of 2D TMDs and nanoscale metals witnesses a boosting development recently, empowering a broad range of applications in optoelectronic devices.

In Table 1, we list and compare the typical architectures of TMDs-nanoscale metals hybrids. From the viewpoint of fabrication, the complexity of the plasmonic hybrids mainly depends on the fabrication methods for the nanoscale metals. The NPs are normally synthesized using chemical methods with a high yield. NPs of different morphologies have been feasibly obtained by controlling the synthesis parameters, and are normally randomly dispersed on/underneath TMDs. NSs are fabricated using physical methods, mostly depend on nanofabrication techniques, they exhibit higher controllability, reproducibility and large-scale periodicity compared with NPs. These advantages could be attributed to the advanced nanofabrication techniques, which in turn, would lead to high costs for the NSs. Placing the NPs or NSs under TMDs is complex than deposition NPs or NSs on the surface of TMDs, because an additional transferring process is needed.

In previous reports, only the semiconducting TMDs (MoS_2, WS_2, $MoSe_2$ and WSe_2) have been used in the fabrication of plasmonic hybrids, as presented in Table 1. Although efficient transfer techniques have been developed [138,139] and applied to stack 2D TMDs toward plasmonic heterostructures, small amount of wrinkles, contamination still cannot avoid. Thus, realizing large area transfer and keeping high quality are still the obstacles, hindering their functionalities and the application potential in large-scale processes.

PL emission is one of the basic optical properties of semiconducting TMDs, so the PL enhancement factor (EF) is a very important criterion to evaluate the plamonic enhancement of the TMDs-nanoscale metals hybrids. It is noteworthy that the PL EF for the hybrid frameworks composed by stacking TMDs on nanoscale metals is much higher than their counterparts that decorated with nanoscale metals on the surface of TMDs. The reported highest EF for TMDs/NSs is 1810 for the WSe_2/Au nanotranches hybrid (Ref. [39]), while the highest EF for TMDs/NPs is 560 for the MoS_2/Ag nanowires bundles (Ref. [76]). For the aspect of light emission range, the applications of plasmonic hybrids are mostly focused on the visible-NIR range because of the specific optical bandgap of TMDs.

In terms of application in devices, the architecture of TMDs/NSs covers the most widely domains of devices, from light emitter, photodetector to THz devices. By involving strain engineering, TMDs/NSs hybrid heterostructures exhibited potential application in the quantum light emitter [36,89,90]. Remarkably, all the reported THz devices were fabricated using the TMDs/NS architecture. Although TMDs exhibited extraordinary nonlinearly optical properties after hybridized with metasurface, their application in devices is not reported yet. The TMDs/metasurface frameworks have proposed a root for room-temperature and free-space nonlinear, quantum and valleytronic nanodevices. It is worthy to note that the sandwich-like architecture of NPs/TMDs/metal film is not employed in the device applications, although it stimulates high PL EF.

Despite the considerable progress and extraordinary application so far, there is still plenty of room to improve the performance of TMDs-nanoscale metals hybrids. The fabrication features of these plasmonic hybrids mainly depends on the characteristics of the nanoscale metals that integrated with TMDs. The density of the effective plamonic nanoscale metals is the key in the usability of devices, and the homogeneity of EF over the device is also important for the practical application of devices. Controllable plamonic coupling, scalable fabrication, and exploring the other TMDs are the pathways to practical applications and commercial manufacture.

The resonance center of LSPRs is desired to be tailored according to the bandgap of TMDs and frequency of excitation, especially for the NIR and THz devices. Therefore, the NSs exhibit significant superiority compared with NPs obtained using chemical methods, because of the controllability, reproducibility and large-scale periodicity. Moreover, from the aspect integrality with silicon technologies and complementary metal−oxide−semiconductor (CMOS) compatibility, directly fabrication NSs on top of TMDs would be a better choice of architecture for commercial devices. However, improving the plamonic enhancement of NSs/TMDs hybrids is called, as the PL EF for the NSs/TMDs hybrids is still much lower than that of TMDs/NSs hybrids.

Scalable fabrication of TMDs-nanoscale metals hybrid nanostructures remains a primary barrier for future commercial device fabrication, which is limited by size of TMDs flake. The TMDs employed to hybridize with plasmonic nanostructures are mostly ME or CVD-grown TMDs, because of their excellent intrinsic optical properties. Although a modified ME method to produce mm sized monolayer TMDs has been proposed [140], it is not satisfy the requirements for commercial integration or manufacturing. Because

Table 1
Comparison of TMDs-metal nanostructure hybrids fabricated with different architecture.

Hybrids	Architecture	Plasmonic Metals in Hybrids	TMDs in Hybrids	Fabrication characteristics		Enhanced PL	Application in Device
				Controllability	Reproducibility	Enhancement Factor	
NPs + TMDs	NPs/TMDs	Chemical synthesized NPs [28–30,33,127,128]	MoS_2, WS_2,	M	M	40 [29]	Photodetector(Vis)
		Shell-isolated nanoparticles [98]	MoS_2			110 [98]	Photodetector(Vis)
		Physical prepared NPs [70–73,115,129,130]	MoS_2, WS_2			28 [70]	Photodetector (NIR)
		Nanowires [31,69,118]	MoS_2, WS_2			20 [69]	Photodetector(Vis)
		Nanorods [32,58,64]	MoS_2, WSe_2,			6.5 [32]	Photocatalyst
	TMDs/NPs	Chemical synthesized NPs [53,74]	MoS_2,	M	M	200 [53]	Photodetector(Vis)
		Nanospheres dimer [79	MoS_2			160 [79]	NA
		Physical prepared NPs [81]	WSe_2			NA	Quantum Light Emitter
		Nanowires [76]	MoS_2			560 [76]	Photodetector(Vis)
NSs + TMDs	NSs/TMDs	Regular arrays [35, 82–83, 110–111, 130]	MoS_2, WS_2	H	H	12 [83]	Photodetector(Vis)
		Nanogap [38, 86]	MoS_2			40 [38]	NA
		Nanostrips [131]	MoS_2			NA	Photodetector (NIR)
	TMDs/NSs	Regular arrays [34, 88, 116]	WS_2, $MoSe_2$,	H	H	3 [34]	Photodetector(Vis)
		Nanogap [89]	WSe_2			200 [89]	Quantum light emitter
		Nanopillar [36, 90]	WSe_2			~7 [36]	Quantum light emitter
		Nanotranches [39, 92, 125]	WSe_2, WS_2			1810 [39]	Nonlinearly optical/ THz devices
		Nanoholes [37, 112]	MoS_2, WS_2			7 [112]	NA
		Metasurface [123–126, 136–137]	WS_2, MoS_2,WSe_2			NA	Nonlinearly optical/ THz devices
		Resonance wire [54]	MoS_2			NA	Photodetector (NIR)
TMDs sandwiched between nanoscale metals	NPs/TMDs/ metal film	Chemical synthesized NPs [65, 102, 117]	WS_2, MoS_2	M	M	NA	NA
		Nanocubes [63]	MoS_2			1200 [63]	NA
		Nanowires [43]	WS_2			3 [43]	NA
	NSs/TMDs/ metal film	Regular arrays [44, 111]	WSe_2, MoS_2	H	H	181 [44]	Quantum Light Emitter
		Nanogap [96]	MoS_2			27.87 [96]	Photocatalyst
		Metasurface [101]	MoS_2			1.6 [101]	NA
	NPs/TMDs/ NSs	Shell-isolated nanoparticles +Periodic disc arrays [98]	MoS_2	M	M	110 [98]	Photodetector(Vis)

L = Low M = Medium H=High.

of the uncontrollable size and thickness of ME TMDs, the devices fabricated using ME TMDs are just prototype for laboratory research to illustrate a possibility for certain applications. To realize widely commercial applications in modern electronics and optoelectronics, uniform wafer-scale growth of TMDs is instrumental target. In recent years, wafer-scale TMDs have been reported using CVD technique [141–143], suggesting that CVD-grown TMDs is a proper candidate for commercial device fabrication. Yet, further improvement is still foreseen in terms of suppressed lattice disorder, decreased grain boundaries for CVD-grown TMDs with higher mobility, and stronger PL emission.

At current stage, due to the bandgap of semiconducting TMDs, most applications of the plasmonic hybrids are limited to visible range and NIR range, and consequently exhibit high optoelectronic responds only at a very narrow wavelength range. Exploring other kinds of TMDs with different electronic structures in the plasmonic hybrids would be a possible path to extend the application domains of hybrids. Moreover, broadening the light-respond range of the hybrids is one approach to improve the efficiency of the optoelectronic devices. In recent years, TMDs heterojunctions composed by stacking a different TMDs layer, or graphene, hexagonal boron nitride (h-BN), black phosphorus (BP), etc. have attracted more attention, due to their tunable electronic and optical properties and associated applications in optoelectronic device [144,145]. However, at current stage, only one type of TMDs is employed in most of the TMDs-nanoscale metals hybrid nanosystems. In the future, plasmonic hybrids based on TMDs heterojunctions may pave a new route for enhanced optoelectronic devices. For example, because graphene has demonstrated the extraordinary application potential in THz devices, graphene/TMDs heterojunction could be a good platform for exploring the application of TMDs-nanoscale metals hybrids in THz devices.

To summary, the outstanding high performance taken together with the advantages of flexibility and integrability with silicon technologies, or CMOS compatibility have lent the plasmonic hybrid nanodevices of TMDs-nanoscale metals a very promising prospect in the next-generation optoelectronics, and remains grand challenges for the practical applications and commercial manufacture.

Declaration of competing interest

The authors declare that they have no known competing financial interests or personal relationships that could have appeared to influence the work reported in this paper.

Acknowledgments

This work was supported by the National Key Research and Development Program of China (grant nos 2018YFB0703500, 2016YFA0200800 and 2016YFA0200400), the National Natural Science Foundation of China (grant nos 11704401, 12074420, 11674387, 91323304, and 61390503), and the Key Deployment Project of Centre for Ocean Mega-Research of Science, Chinese Academy of Sciences (grant no. COMS2020J03).

References

[1] B. Radisavljevic, A. Radenovic, J. Brivio, V. Giacometti, A. Kis, Single-layer Mos_2 transistors, Nat. Nanotechnol. 6 (2011) 147–150.
[2] W. Zheng, Y. Jiang, X. Hu, H. Li, Z. Zeng, X. Wang, A. Pan, Light emission properties of 2d transition metal dichalcogenides: fundamentals and applications, Adv. Opt. Mater. 6 (2018) 1800420.
[3] J. Zhou, J. Lin, X. Huang, Y. Zhou, Y. Chen, J. Xia, H. Wang, Y. Xie, H. Yu, J. Lei, A library of atomically thin metal chalcogenides, Nature 556 (2018) 355–359.
[4] N. Mounet, M. Gibertini, P. Schwaller, D. Campi, A. Merkys, A. Marrazzo, T. Sohier, I.E. Castelli, A. Cepellotti, G. Pizzi, Two-dimensional materials from high-throughput computational exfoliation of experimentally known compounds, Nat. Nanotechnol. 13 (2018) 246–252.
[5] A. Ramasubramaniam, Large excitonic effects in monolayers of molybdenum and tungsten dichalcogenides, Phys. Rev. B 86 (2012) 115409.
[6] J. Pu, T. Takenobu, Monolayer transition metal dichalcogenides as light sources, Adv. Mater. 30 (2018) 1707627.
[7] N. Huo, G. Konstantatos, Recent progress and future prospects of 2d-based photodetectors, Adv. Mater. 30 (2018) 1801164.
[8] G. Wang, Y. Zhang, C. You, B. Liu, Y. Yang, H. Li, A. Cui, D. Liu, H. Yan, Two dimensional materials based photodetectors, Infrared Phys. Technol. 88 (2018) 149–173.
[9] Z. Sun, A. Martinez, F. Wang, Optical modulators with 2d layered materials, Nat. Photon. 10 (2016) 227–238.
[10] A.C. Ferrari, F. Bonaccorso, V. Fal'Ko, K.S. Novoselov, S. Roche, P. Bøggild, S. Borini, F.H. Koppens, V. Palermo, N. Pugno, Science and technology roadmap for graphene, related two-dimensional crystals, and hybrid systems, Nanoscale 7 (2015) 4598–4810.
[11] A. Grigorenko, M. Polini, K. Novoselov, Graphene plasmonics, Nat. Photonics. 6 (2012) 749–758.
[12] J.R. Piper, S. Fan, Broadband Absorption enhancement in solar cells with an atomically thin active layer, ACS Photonics 3 (2016) 571–577.
[13] R.R. Nair, P. Blake, A.N. Grigorenko, K.S. Novoselov, T.J. Booth, T. Stauber, N.M. Peres, A.K. Geim, Fine structure constant defines visual transparency of graphene, Science 320 (2008), 1308-1308.
[14] S.T. Kochuveedu, Y.H. Jang, D.H. Kim, A study on the mechanism for the interaction of light with noble metal-metal oxide semiconductor nanostructures for various photophysical applications, Chem. Soc. Rev. 42 (2013) 8467–8493.
[15] X. Gu, T. Qiu, W. Zhang, P.K. Chu, Light-emitting diodes enhanced by localized surface plasmon resonance, Nanoscale. Res. Lett. 6 (2011) 199.
[16] R. Jiang, B. Li, C. Fang, J. Wang, Metal/semiconductor hybrid nanostructures for plasmon-enhanced applications, Adv. Mater. 26 (2014) 5274–5309.
[17] Y. Li, Z. Li, C. Chi, H. Shan, L. Zheng, Z. Fang, Plasmonics of 2d nanomaterials: properties and applications, Adv. Sci. 4 (2017) 1600430.
[18] Z. Cai, Y. Xu, C. Wang, Y. Liu, Polariton photonics using structured metals and 2d materials, Adv. Opt. Mater. 8 (2020) 1901090.
[19] M. Cotrufo, L. Sun, J. Choi, A. Alù, X. Li, Enhancing functionalities of atomically thin semiconductors with plasmonic nanostructures, Nanophotonics 8 (2019) 577–598.
[20] P. Sriram, A. Manikandan, F.C. Chuang, Y.L. Chueh, Hybridizing plasmonic materials with 2d-transition metal dichalcogenides toward functional applications, Small 16 (2020) 1904271.
[21] X. Li, J. Zhu, B. Wei, Hybrid nanostructures of metal/two-dimensional nanomaterials for plasmon-enhanced applications, Chem. Soc. Rev. 45 (2016) 3145–3187.
[22] F. Schwierz, J. Pezoldt, R. Granzner, Two-dimensional materials and their prospects in transistor electronics, Nanoscale 7 (2015) 8261–8283.
[23] Y.M. Shi, H.N. Li, L.J. Li, Recent advances in controlled synthesis of two-dimensional transition metal dichalcogenides via vapour deposition techniques, Chem. Soc. Rev. 44 (2015) 2744–2756.
[24] W. Choi, N. Choudhary, G.H. Han, J. Park, D. Akinwande, Y.H. Lee, Recent development of two-dimensional transition metal dichalcogenides and their applications. *Mater*, Today Off. 20 (2017) 116–130.
[25] B. Radisavljevic, A. Radenovic, J. Brivio, V. Giacometti, A. Kis, Single-layer MoS_2 transistors, Nat. Nanotechnol. 6 (2011) 147–150.
[26] M.S. Fuhrer, J. Hone, Measurement of mobility in dual-gated Mos2 transistors, Nat. Nanotechnol. 8 (2013) 146–147.
[27] K. Kang, S.E. Xie, L.J. Huang, Y.M. Han, P.Y. Huang, K.F. Mak, C.J. Kim, D. Muller, J. Park, High-mobility three-atom-thick semiconducting films with wafer-scale homogeneity, Nature 520 (2015) 656–660.
[28] J. Yan, C. Ma, P. Liu, G. Yang, Plasmon-induced energy transfer and photoluminescence manipulation in MoS_2 with a different number of layers, ACS Photonics 4 (2017) 1092–1100.
[29] T.S. Bhattacharya, S. Mitra, S.S. Singha, P.K. Mondal, A. Singha, Tailoring light-matter interaction in WS_2–gold nanoparticles hybrid systems, Phys. Rev. B 100 (2019) 235438.
[30] W. Gao, Y.H. Lee, R. Jiang, J. Wang, T. Liu, X.Y. Ling, Localized and continuous tuning of monolayer MoS_2 photoluminescence using a single shape-controlled Ag nanoantenna, Adv. Mater. 28 (2016) 701–706.
[31] E. Palacios, S. Park, L. Lauhon, K. Aydin, Identifying excitation and emission rate contributions to plasmon-enhanced photoluminescence from monolayer MoS_2 using a tapered gold nanoantenna, ACS Photonics 4 (2017) 1602–1606.
[32] K.C. Lee, Y.-H. Chen, H.-Y. Lin, C.-C. Cheng, P.-Y. Chen, T.-Y. Wu, M.-H. Shih, K.-H. Wei, L.-J. Li, C.-W. Chang, Plasmonic gold nanorods coverage influence on enhancement of the photoluminescence of two-dimensional MoS_2 monolayer, Sci. Rep. 5 (2015) 16374.
[33] S. Diefenbach, E. Parzinger, J. Kiemle, J. Wierzbowski, S. Funke, B. Miller, R.k. Csiki, P. Thiesen, A. Cattani-Scholz, U. Wurstbauer, Manifold coupling mechanisms of transition metal dichalcogenides to plasmonic gold nanoparticle arrays, J. Phys. Chem. C 122 (2018) 9663–9670.
[34] S. Najmaei, A. Mlayah, A. Arbouet, C. Girard, J. Leotin, J. Lou, Plasmonic pumping of excitonic photoluminescence in hybrid MoS_2–Au nanostructures, ACS Nano 8 (2014) 12682–12689.
[35] J. Li, Q. Ji, S. Chu, Y. Zhang, Y. Li, Q. Gong, K. Liu, K. Shi, Tuning the photoresponse in monolayer MoS_2 by plasmonic nano-antenna, Sci. Rep. 6 (2016) 1–7.
[36] T. Cai, J.-H. Kim, Z. Yang, S. Dutta, S. Aghaeimeibodi, E. Waks, Radiative enhancement of single quantum emitters in WSe_2 monolayers using site-controlled metallic nanopillars, ACS Photonics 5 (2018) 3466–3471.
[37] W.-B. Shi, L. Zhang, D. Wang, R.-L. Zhang, Y. Zhu, L.-H. Zhang, R. Peng, W. Bao, R.-H. Fan, M. Wang, Hybrid coupling enhances photoluminescence of monolayer MoS_2 on plasmonic nanostructures, Opt. Lett. 43 (2018) 4128–4131.
[38] B. Lee, J. Park, G.H. Han, H.-S. Ee, C.H. Naylor, W. Liu, A.C. Johnson, R. Agarwal, Fano resonance and spectrally modified photoluminescence enhancement in monolayer MoS2 integrated with plasmonic nanoantenna array, Nano Lett. 15 (2015) 3646–3653.
[39] Z. Wang, Z. Dong, Y. Gu, Y.-H. Chang, L. Zhang, L.-J. Li, W. Zhao, G. Eda, W. Zhang, G. Grinblat, Giant photoluminescence enhancement in tungsten-diselenide–gold plasmonic hybrid structures, Nat. Commun. 7 (2016) 1–8.
[40] H. Chen, L. Shao, Q. Li, J. Wang, Gold nanorods and their plasmonic properties, Chem. Soc. Rev. 42 (2013) 2679–2724.
[41] M.S. Sander, L.S. Tan, Nanoparticle arrays on surfaces fabricated using anodic alumina films as templates, Adv. Funct. Mater. 13 (2003) 393–397.
[42] X. Zhang, C.R. Yonzon, R.P. Van Duyne, Nanosphere lithography fabricated plasmonic materials and their applications, J. Mater. Res. 21 (2006) 1083–1092.
[43] F. Cheng, A.D. Johnson, Y. Tsai, P.-H. Su, S. Hu, J.G. Ekerdt, C.-K. Shih, Enhanced photoluminescence of monolayer WS_2 on Ag films and nanowire–WS_2–film composites, ACS Photonics 4 (2017) 1421–1430.
[44] Y. Luo, G.D. Shepard, J.V. Ardelean, D.A. Rhodes, B. Kim, K. Barmak, J.C. Hone, S. Strauf, Deterministic coupling of site-controlled quantum emitters in monolayer Wse 2 to plasmonic nanocavities, Nat. Nanotechnol. 13 (2018) 1137–1142.
[45] G. Eda, S.A. Maier, Two-dimensional crystals: managing light for optoelectronics, ACS Nano 7 (2013) 5660–5665.
[46] E. Le Ru, P. Etchegoin, Principles of Surface-Enhanced Raman Spectroscopy: and Related Plasmonic Effects, Elsevier, 2008.
[47] S.-Y. Ding, E.-M. You, Z.-Q. Tian, M. Moskovits, Electromagnetic theories of surface-enhanced Raman spectroscopy, Chem. Soc. Rev. 46 (2017) 4042–4076.
[48] S.-Y. Ding, J. Yi, J.-F. Li, B. Ren, D.-Y. Wu, R. Panneerselvam, Z.-Q. Tian, Nanostructure-based plasmon-enhanced Raman spectroscopy for surface analysis of materials, Nat. Rev. Mater. 1 (2016) 1–16.
[49] E.M. Purcell, H.C. Torrey, R.V. Pound, Resonance absorption by nuclear magnetic moments in a solid, Phys. Rev. 69 (1946) 37.
[50] V. Giannini, A.I. Fernández-Domínguez, S.C. Heck, S.A. Maier, Plasmonic nanoantennas: fundamentals and their use in controlling the radiative properties of nanoemitters, Chem. Rev. 111 (2011) 3888–3912.
[51] G. Sun, J. Khurgin, R. Soref, Plasmonic light-emission enhancement with isolated metal nanoparticles and their coupled arrays, J. Opt. Soc. Am. B 25 (2008) 1748–1755.
[52] K. Okamoto, I. Niki, A. Shvartser, Y. Narukawa, T. Mukai, A. Scherer, Surface-plasmon-enhanced light emitters based on ingan quantum wells, Nat. Mater. 3 (2004) 601–605.
[53] Y. Zeng, X. Li, W. Chen, J. Liao, J. Lou, Q. Chen, Highly enhanced photoluminescence of monolayer Mos2 with self-assembled Au nanoparticle arrays, Adv. Mater. Interfaces. 4 (2017) 1700739.
[54] W. Wang, A. Klots, D. Prasai, Y. Yang, K.I. Bolotin, J. Valentine, Hot electron-based near-infrared photodetection using bilayer MoS_2, Nano Lett. 15 (2015) 7440–7444.
[55] J. Zhang, P. Wang, J. Sun, Y. Jin, High-efficiency plasmon-enhanced and graphene-supported semiconductor/metal core–satellite hetero-nanocrystal photocatalysts for visible-light dye photodegradation and H_2 production from water, ACS Appl. Mater. Interfaces 6 (2014) 19905–19913.
[56] D.O. Sigle, L. Zhang, S. Ithurria, B. Dubertret, J.J. Baumberg, Ultrathin CdSe in plasmonic nanogaps for enhanced photocatalytic water splitting, J. Phys. Chem. Lett. 6 (2015) 1099–1103.
[57] C. Clavero, Plasmon-induced hot-electron generation at nanoparticle/metal-oxide interfaces for photovoltaic and photocatalytic devices, Nat. Photon. 8 (2014) 95–103.
[58] Y. Kang, Y. Gong, Z. Hu, Z. Li, Z. Qiu, X. Zhu, P.M. Ajayan, Z. Fang, Plasmonic hot electron enhanced MoS_2 photocatalysis in hydrogen evolution, Nanoscale 7 (2015) 4482–4488.
[59] X. Wen, W. Xu, W. Zhao, J.B. Khurgin, Q. Xiong, Plasmonic hot carriers-controlled second harmonic generation in WSe_2 bilayers, Nano Lett. 18

(2018) 1686–1692.
[60] P. Nordlander, E. Prodan, Plasmon hybridization in nanoparticles near metallic surfaces, Nano Lett. 4 (2004) 2209–2213.
[61] P.T. Bowen, D.R. Smith, Coupled-mode theory for film-coupled plasmonic nanocubes, Phys. Rev. B 90 (2014) 195402.
[62] C. Tserkezis, R. Esteban, D.O. Sigle, J. Mertens, L.O. Herrmann, J.J. Baumberg, J. Aizpurua, Hybridization of plasmonic antenna and cavity modes: extreme optics of nanoparticle-on-mirror nanogaps, Phys. Rev. A 92 (2015): 053811.
[63] J. Huang, G.M. Akselrod, T. Ming, J. Kong, M.H. Mikkelsen, Tailored emission spectrum of 2D semiconductors using plasmonic nanocavities, ACS Photonics 5 (2018) 552–558.
[64] D. Zheng, S. Zhang, Q. Deng, M. Kang, P. Nordlander, H. Xu, Manipulating coherent plasmon–exciton interaction in a single silver nanorod on monolayer WSe_2, Nano Lett. 17 (2017) 3809–3814.
[65] X. Han, K. Wang, X. Xing, M. Wang, P. Lu, Rabi splitting in a plasmonic nanocavity coupled to a WS_2 monolayer at room temperature, ACS Photonics 5 (2018) 3970–3976.
[66] W. Liu, B. Lee, C.H. Naylor, H.-S. Ee, J. Park, A.C. Johnson, R. Agarwal, Strong exciton–plasmon coupling in MoS_2 coupled with plasmonic lattice, Nano Lett. 16 (2016) 1262–1269.
[67] W. Liu, Y. Wang, C.H. Naylor, B. Lee, B. Zheng, G. Liu, A.C. Johnson, A. Pan, R. Agarwal, Understanding the different exciton–plasmon coupling regimes in two-dimensional semiconductors coupled with plasmonic lattices: a combined experimental and unified equation of motion approach, ACS Photonics 5 (2018) 192–204.
[68] S.-H. Gong, F. Alpeggiani, B. Sciacca, E.C. Garnett, L. Kuipers, Nanoscale chiral valley-photon interface through optical spin-orbit coupling, Science 359 (2018) 443–447.
[69] H.S. Lee, M.S. Kim, Y. Jin, G.H. Han, Y.H. Lee, J. Kim, Selective amplification of the primary exciton in a MoS_2 monolayer, Phys. Rev. Lett. 115 (2015) 226801.
[70] L. Gong, Q. Zhang, L. Wang, J. Wu, C. Han, B. Lei, W. Chen, G. Eda, K.E.J. Goh, C.H. Sow, Emergence of photoluminescence on bulk MoS_2 by laser thinning and gold particle decoration, Nano. Res. 11 (2018) 4574–4586.
[71] Y. Lei, D. Li, T.C. Zhang, X. Huang, L. Liu, Y. Lu, One-step selective formation of silver nanoparticles on atomic layered MoS_2 by laser-induced defect engineering and photoreduction, J. Mater. Chem. C 5 (2017) 8883–8892.
[72] W. Zhao, S. Wang, B. Liu, I. Verzhbitskiy, S. Li, F. Giustiniano, D. Kozawa, K.P. Loh, K. Matsuda, K. Okamoto, Exciton–plasmon coupling and electromagnetically induced transparency in monolayer semiconductors hybridized with Ag nanoparticles, Adv. Mater. 28 (2016) 2709–2715.
[73] F. Wang, H. Xu, J. Fang, G. Wang, X. Zhang, Probing the interfacial interaction between monolayer molybdenum disulfide and Au nanoclusters, Surf. Interface Anal. 49 (2017) 858–863.
[74] M.-G. Lee, S. Yoo, T. Kim, Q.-H. Park, Large-area plasmon enhanced two-dimensional MoS_2, Nanoscale 9 (2017) 16244–16248.
[75] C. Obiakara, M.A. Mahmoud, Electromagnetic plasmonic field of nanoparticles tune the band gap of two-dimensional semiconducting materials, J. Mater. Chem. C 7 (2019) 3675–3687.
[76] S. Bang, N.T. Duong, J. Lee, Y.H. Cho, H.M. Oh, H. Kim, S.J. Yun, C. Park, M.-K. Kwon, J.-Y.J.N.L. Kim, Augmented quantum yield of a 2D monolayer photodetector by surface plasmon coupling, Nano Lett. 18 (2018) 2316–2323.
[77] T. Cai, S. Dutta, S. Aghaeimeibodi, Z. Yang, S. Nah, J.T. Fourkas, E. Waks, Coupling emission from single localized defects in two-dimensional semiconductor to surface plasmon polaritons, Nano Lett. 17 (2017) 6564–6568.
[78] G. Braun, I. Pavel, A.R. Morrill, D.S. Seferos, G.C. Bazan, N.O. Reich, M. Moskovits, Chemically patterned microspheres for controlled nanoparticle assembly in the construction of sers hot spots, J. Am. Chem. Soc. 129 (2007) 7760–7761.
[79] Q. Hao, J. Pang, Y. Zhang, J. Wang, L. Ma, O.G. Schmidt, Boosting the photoluminescence of monolayer MoS_2 on high-density nanodimer arrays with sub-10 nm gap, Adv. Opt. Mater. 6 (2018) 1700984.
[80] B. Ding, Z. Zhang, Y.-H. Chen, Y. Zhang, R.J. Blaikie, M. Qiu, Tunable valley polarized plasmon-exciton polaritons in two-dimensional semiconductors, ACS Nano 13 (2019) 1333–1341.
[81] L.N. Tripathi, O. Iff, S. Betzold, Ł. Dusanowski, M. Emmerling, K. Moon, Y.J. Lee, S.-H. Kwon, S. Höfling, C. Schneider, Spontaneous emission enhancement in strain-induced WSe_2 monolayer-based quantum light sources on metallic surfaces, ACS Photonics 5 (2018) 1919–1926.
[82] H. Taghinejad, S.H. Shams-Mousavi, Y. Gong, M. Taghinejad, A.A. Eftekhar, P. Ajayan, A. Adibi, Lattice plasmon induced large enhancement of excitonic emission in monolayer metal dichalcogenides, Plasmonics 12 (2017) 1975–1981.
[83] S. Butun, S. Tongay, K. Aydin, Enhanced light emission from large-area monolayer MoS_2 using plasmonic nanodisc arrays, Nano Lett. 15 (2015) 2700–2704.
[84] J.-M. Nam, J.-W. Oh, H. Lee, Y.D. Suh, Plasmonic nanogap-enhanced Raman scattering with nanoparticles, Acc. Chem. Res. 49 (2016) 2746–2755.
[85] Y. Yang, C. Gu, J. Li, Sub-5 nm metal nanogaps: physical properties, fabrication methods, and device applications, Small 15 (2019) 1804177.
[86] E. Palacios, S. Park, S. Butun, L. Lauhon, K. Aydin, Enhanced radiative emission from monolayer MoS_2 films using a single plasmonic dimer nanoantenna, Appl. Phys. Lett. 111 (2017): 031101.
[87] S. Dutta, T. Cai, M.A. Buyukkaya, S. Barik, S. Aghaeimeibodi, E. Waks, Coupling quantum emitters in WSe_2 monolayers to a metal-insulator-metal waveguide, Appl. Phys. Lett. 113 (2018) 191105.
[88] H. Chen, J. Yang, E. Rusak, J. Straubel, R. Guo, Y.W. Myint, J. Pei, M. Decker, I. Staude, C. Rockstuhl, Manipulation of photoluminescence of two-dimensional $MoSe_2$ by gold nanoantennas, Sci. Rep. 6 (2016) 22296.
[89] A.D. Johnson, F. Cheng, Y. Tsai, C.-K. Shih, Giant enhancement of defect-bound exciton luminescence and suppression of band-edge luminescence in monolayer WSe_2–Ag plasmonic hybrid structures, Nano Lett. 17 (2017) 4317–4322.
[90] O. Iff, N. Lundt, S. Betzold, L.N. Tripathi, M. Emmerling, S. Tongay, Y.J. Lee, S.-H. Kwon, S. Höfling, C. Schneider, Deterministic coupling of quantum emitters in WSe_2 monolayers to plasmonic nanocavities, Optic Express 26 (2018) 25944–25951.
[91] Y. Yu, Z. Ji, S. Zu, B. Du, Y. Kang, Z. Li, Z. Zhou, K. Shi, Z. Fang, Ultrafast plasmonic hot electron transfer in Au nanoantenna/MoS_2 heterostructures, Adv. Funct. Mater. 26 (2016) 6394–6401.
[92] M.S. Eggleston, S.B. Desai, K. Messer, S.A. Fortuna, S. Madhvapathy, J. Xiao, X. Zhang, E. Yablonovitch, A. Javey, M.C. Wu, Ultrafast spontaneous emission from a slot-antenna coupled WSe_2 monolayer, ACS Photonics 5 (2018) 2701–2705.
[93] I. Song, C. Park, M. Hong, J. Baik, H.-J. Shin, H.C. Choi, Patternable large-scale molybdenium disulfide atomic layers grown by gold-assisted chemical vapor deposition, Angew. Chem. Int. Ed. 53 (2014) 1266–1269.
[94] R. Ma, M.J. Haastrup, Z.G. Wang, Y.M. Liu, H. Ye, M.D. Dong, J.V. Lauritsen, D.S. Sutherland, Direct integration of few-layer MoS_2 at plasmonic Au nanostructure by substrate-diffusion delivered Mo, Adv. Mater. Interfaces 7 (2020).
[95] L. Yu, D. Liu, X.-Z. Qi, X. Xiong, L.-T. Feng, M. Li, G.-P. Guo, G.-C. Guo, X.-F. Ren, Gap plasmon-enhanced photoluminescence of monolayer MoS_2 in hybrid nanostructure, Chin. Phys. B 27 (2018): 047302.
[96] P. Sriram, D.S. Su, A.P. Periasamy, A. Manikandan, S.W. Wang, H.T. Chang, Y.L. Chueh, T.J. Yen, Hybridizing strong quadrupole gap plasmons using optimized nanoantennas with bilayer MoS_2 for excellent photo-electrochemical hydrogen evolution, Adv. Energy Mater. 8 (2018) 1801184.
[97] J.F. Li, X.D. Tian, S.B. Li, J.R. Anema, Z.L. Yang, Y. Ding, Y.F. Wu, Y.M. Zeng, Q.Z. Chen, B. Ren, Surface analysis using shell-isolated nanoparticle-enhanced Raman spectroscopy, Nat. Protoc. 8 (2013) 52.
[98] Z.Q. Wu, J.L. Yang, N.K. Manjunath, Y.J. Zhang, S.R. Feng, Y.H. Lu, J.H. Wu, W.W. Zhao, C.Y. Qiu, J.F. Li, Gap-mode surface-plasmon-enhanced photoluminescence and photoresponse of MoS_2, Adv. Mater. 30 (2018) 1706527.
[99] K.F. Mak, K. He, J. Shan, T.F. Heinz, Control of valley polarization in monolayer MoS_2 by optical helicity, Nat. Nanotechnol. 7 (2012) 494–498.
[100] T. Cao, G. Wang, W. Han, H. Ye, C. Zhu, J. Shi, Q. Niu, P. Tan, E. Wang, B. Liu, Valley-selective circular dichroism of monolayer molybdenum disulphide, Nat. Commun. 3 (2012) 1–5.
[101] Z. Li, C. Liu, X. Rong, Y. Luo, H. Cheng, L. Zheng, F. Lin, B. Shen, Y. Gong, S. Zhang, Tailoring MoS_2 valley-polarized photoluminescence with super chiral near-field, Adv. Mater. 30 (2018) 1801908.
[102] Z. Li, Y. Xiao, Y. Gong, Z. Wang, Y. Kang, S. Zu, P.M. Ajayan, P. Nordlander, Z. Fang, Active light control of the MoS_2 monolayer exciton binding energy, ACS Nano 9 (2015) 10158–10164.
[103] M. Wang, Z. Wu, A. Krasnok, T. Zhang, M. Liu, H. Liu, L. Scarabelli, J. Fang, L.M. Liz-Marzán, M. Terrones, Dark-exciton-mediated Fano resonance from a single gold nanostructure on monolayer WS_2 at room temperature, Small 15 (2019) 1900982.
[104] S. Kena-Cohen, S.R. Forrest, Room-temperature polariton lasing in an organic single-crystal microcavity, Nat. Photon. 4 (2010) 371–375.
[105] K. Hennessy, A. Badolato, M. Winger, D. Gerace, M. Atature, S. Gulde, S. Falt, E.L. Hu, A. Imamoglu, Quantum nature of a strongly coupled single quantum dot-cavity system, Nature 445 (2007) 896–899.
[106] F. Nan, Y.F. Zhang, X.G. Li, X.T. Zhang, H. Li, X.H. Zhang, R.B. Jiang, J.F. Wang, W. Zhang, L. Zhou, J.H. Wang, Q.Q. Wang, Z.Y. Zhang, Unusual and tunable one-photon nonlinearity in gold-dye plexcitonic Fano systems, Nano Lett. 15 (2015) 2705–2710.
[107] G. Khitrova, H.M. Gibbs, M. Kira, S.W. Koch, A. Scherer, Vacuum Rabi splitting in semiconductors, Nat. Phys. 2 (2006) 81–90.
[108] C.X. Cong, J.Z. Shang, Y.L. Wang, T. Yu, Optical properties of 2D semiconductor WS_2, Adv. Opt. Mater. 6 (2018).
[109] J. Xiao, M. Zhao, Y. Wang, X. Zhang, Excitons in atomically thin 2D semiconductors and their applications, Nanophotonics 6 (2017) 1309–1328.
[110] S. Butun, E. Palacios, J.D. Cain, Z. Liu, V.P. Dravid, K. Aydin, Quantifying plasmon-enhanced light absorption in monolayer WS_2 films, ACS Appl. Mater. Interfaces 9 (2017) 15044–15051.
[111] S. Zu, B. Li, Y. Gong, Z. Li, P.M. Ajayan, Z. Fang, Active control of plasmon–exciton coupling in MoS_2–Ag hybrid nanostructures, Adv. Opt. Mater. 4 (2016) 1463–1469.
[112] X. Chen, H. Wang, N.-S. Xu, H. Chen, S. Deng, Resonance coupling in hybrid gold nanohole–monolayer WS_2 nanostructures, Appl. Mater. Today. 15 (2019) 145–152.
[113] H. Zhou, F. Yu, C.F. Guo, Z. Wang, Y. Lan, G. Wang, Z. Fang, Y. Liu, S. Chen, L. Sun, Well-oriented epitaxial gold nanotriangles and bowties on MoS_2 for surface-enhanced Raman scattering, Nanoscale 7 (2015) 9153–9157.
[114] G. Sharma, A. Singh, R. Sharma, B.P. Singh, P. Vasa, Strain and plasmonic field induced modifications of material excitation response in monolayer MoS_2, J. Appl. Phys. 125 (2019): 063101.

[115] D. Zhang, Y.-C. Wu, M. Yang, X. Liu, C.Ó. Coileáin, M. Abid, M. Abid, J.-J. Wang, I. Shvets, H. Xu, Surface enhanced Raman scattering of monolayer MX_2 with metallic nano particles, Sci. Rep. 6 (2016) 1–8.
[116] W. Yang, H. Li, J. Chen, J. Yin, J. Li, Y. Wu, B. Mo, T. Wu, B. Sun, Z. Wu, Plasmon-enhanced exciton emissions and Raman scattering of cvd-grown monolayer WS_2 on Ag nanoprism arrays, Appl. Surf. Sci. 504 (2020) 144252.
[117] W. Chen, S. Zhang, M. Kang, W. Liu, Z. Ou, Y. Li, Y. Zhang, Z. Guan, H. Xu, Probing the limits of plasmonic enhancement using a two-dimensional atomic crystal probe, Light Sci. Appl. 7 (2018) 1–11.
[118] Q. Guo, T. Fu, J. Tang, D. Pan, S. Zhang, H. Xu, Routing a chiral Raman signal based on spin-orbit interaction of light, Phys. Rev. Lett. 123 (2019) 183903.
[119] Y. Kang, S. Najmaei, Z. Liu, Y. Bao, Y. Wang, X. Zhu, N.J. Halas, P. Nordlander, P.M. Ajayan, J. Lou, Plasmonic hot electron induced structural phase transition in a MoS_2 monolayer, Adv. Mater. 26 (2014) 6467–6471.
[120] F. Spreyer, R. Zhao, L. Huang, T. Zentgraf, Second harmonic imaging of plasmonic pancharatnam-berry phase metasurfaces coupled to monolayers of WS_2, Nanophotonics 9 (2020) 351–360.
[121] X. Hong, G. Hu, W. Zhao, K. Wang, S. Sun, R. Zhu, J. Wu, W. Liu, K.P. Loh, A.T.S. Wee, Structuring nonlinear wavefront emitted from monolayer transition-metal dichalcogenides, Research 2020 (2020) 9085782.
[122] P.K. Jha, N. Shitrit, X. Ren, Y. Wang, X. Zhang, Spontaneous exciton valley coherence in transition metal dichalcogenide monolayers interfaced with an anisotropic metasurface, Phys. Rev. Lett. 121 (2018) 116102.
[123] J. Chen, K. Wang, H. Long, X. Han, H. Hu, W. Liu, B. Wang, P. Lu, Tungsten disulfide–gold nanohole hybrid metasurfaces for nonlinear metalenses in the visible region, Nano Lett. 18 (2018) 1344–1350.
[124] G. Hu, X. Hong, K. Wang, J. Wu, H.-X. Xu, W. Zhao, W. Liu, S. Zhang, F. Garcia-Vidal, B. Wang, Coherent steering of nonlinear chiral valley photons with a synthetic Au–WS_2 metasurface, Nat. Photon. 13 (2019) 467–472.
[125] J. Shi, W.Y. Liang, S.S. Raja, Y. Sang, X.Q. Zhang, C.A. Chen, Y. Wang, X. Yang, Y.H. Lee, H. Ahn, Plasmonic enhancement and manipulation of optical nonlinearity in monolayer tungsten disulfide, Laser Photon. Rev. 12 (2018) 1800188.
[126] W.-P. Guo, W.-Y. Liang, C.-W. Cheng, W.-L. Wu, Y.-T. Wang, Q. Sun, S. Zu, H. Misawa, P.-J. Cheng, S.-W. Chang, Chiral second-harmonic generation from monolayer WS_2/aluminum plasmonic vortex metalens, Nano Lett. 20 (2020) 2857–2864.
[127] J. Lin, H. Li, H. Zhang, W. Chen, Plasmonic enhancement of photocurrent in MoS_2 field-effect-transistor, Appl. Phys. Lett. 102 (2013) 203109.
[128] Y. Liu, W. Huang, W. Chen, X. Wang, J. Guo, H. Tian, H. Zhang, Y. Wang, B. Yu, T.-L. Ren, Plasmon resonance enhanced WS_2 photodetector with ultra-high sensitivity and stability, Appl. Surf. Sci. 481 (2019) 1127–1132.
[129] J. Li, C. Nie, F. Sun, L. Tang, Z. Zhang, J. Zhang, Y. Zhao, J. Shen, S. Feng, H. Shi, Enhancement of the photoresponse of monolayer MoS_2 photodetectors induced by a nanoparticle grating, ACS Appl. Mater. Interfaces 12 (2020) 8429–8436.
[130] J. Miao, W. Hu, Y. Jing, W. Luo, L. Liao, A. Pan, S. Wu, J. Cheng, X. Chen, W. Lu, Surface plasmon-enhanced photodetection in few layer MoS_2 phototransistors with Au nanostructure arrays, Small 11 (2015) 2392–2398.
[131] R. Kumar, A. Sharma, M. Kaur, S. Husale, Pt-Nanostrip-Enabled plasmonically enhanced broad spectral photodetection in bilayer MoS_2, Adv. Opt. Mater. 5 (2017) 1700009.
[132] J. Guo, S. Li, Z. He, Y. Li, Z. Lei, Y. Liu, W. Huang, T. Gong, Q. Ai, L. Mao, Near-infrared photodetector based on few-layer MoS_2 with sensitivity enhanced by localized surface plasmon resonance, Appl. Surf. Sci. 483 (2019) 1037–1043.
[133] G. Wang, L. Li, W. Fan, R. Wang, S. Zhou, J.T. Lü, L. Gan, T. Zhai, Interlayer coupling induced infrared response in WS_2/MoS_2 heterostructures enhanced by surface plasmon resonance, Adv. Funct. Mater. 28 (2018) 1800339.
[134] P. Gopalan, B. Sensale-Rodriguez, 2D materials for terahertz modulation, Adv. Opt. Mater. 8 (2020) 1900550.
[135] J. Shi, Z. Li, D.K. Sang, Y. Xiang, J. Li, S. Zhang, H. Zhang, Thz photonics in two dimensional materials and metamaterials: properties, devices and prospects, J. Mater. Chem. C 6 (2018) 1291–1306.
[136] Y.K. Srivastava, A. Chaturvedi, M. Manjappa, A. Kumar, G. Dayal, C. Kloc, R. Singh, MoS_2 for ultrafast all-optical switching and modulation of thz Fano metaphotonic devices, Adv. Opt. Mater. 5 (2017) 1700762.
[137] Y. Hu, T. Jiang, J. Zhou, H. Hao, H. Sun, H. Ouyang, M. Tong, Y. Tang, H. Li, J. You, Ultrafast terahertz transmission/group delay switching in photoactive WSe_2-functionalized metaphotonic devices, Nanomater. Energy 68 (2020) 104280.
[138] L. Gao, G.-X. Ni, Y. Liu, B. Liu, A.H.C. Neto, K.P. Loh, Face-to-Face transfer of wafer-scale graphene films, Nature 505 (2014) 190–194.
[139] H.D. Phan, Y. Kim, J. Lee, R. Liu, Y. Choi, J.H. Cho, C. Lee, Ultraclean and direct transfer of a wafer-scale MoS_2 thin film onto a plastic substrate, Adv. Mater. 29 (2017) 1603928.
[140] Y. Huang, E. Sutter, N.N. Shi, J. Zheng, T. Yang, D. Englund, H.-J. Gao, P. Sutter, Reliable exfoliation of large-area high-quality flakes of graphene and other two-dimensional materials, ACS Nano 9 (2015) 10612–10620.
[141] H. Yu, M. Liao, W. Zhao, G. Liu, X. Zhou, Z. Wei, X. Xu, K. Liu, Z. Hu, K. Deng, Wafer-scale growth and transfer of highly-oriented monolayer MoS_2 continuous films, ACS Nano 11 (2017) 12001–12007.
[142] X. Li, W. Cai, J. An, S. Kim, J. Nah, D. Yang, R. Piner, A. Velamakanni, I. Jung, E. Tutuc, Large-area synthesis of high-quality and uniform graphene films on copper foils, Science 324 (2009) 1312–1314.
[143] S. Rahimi, L. Tao, S.F. Chowdhury, S. Park, A. Jouvray, S. Buttress, N. Rupesinghe, K. Teo, D. Akinwande, Toward 300 mm wafer-scalable high-performance polycrystalline chemical vapor deposited graphene transistors, ACS Nano 8 (2014) 10471–10479.
[144] X. Zhou, X. Hu, J. Yu, S. Liu, Z. Shu, Q. Zhang, H. Li, Y. Ma, H. Xu, T. Zhai, 2D layered material-based van der Waals heterostructures for optoelectronics, Adv. Funct. Mater. 28 (2018) 1706587.
[145] W. Zhang, Q. Wang, Y. Chen, Z. Wang, A.T. Wee, Van der Waals stacked 2D layered materials for optoelectronics, 2D Mater. 3 (2016): 022001.